POLITECNICO DI TORINO

Master Degree course in Energy and Nuclear Engineering

Master Degree Thesis

Analysis of the Field Quality in Bent Superconducting Magnets for Hadrontherapy Gantries

Supervisors
Prof. Gianni Coppa
Dott. Marco Pullia
Dott. Enrico Felcini

Candidate
Marika D'Addazio

Academic Year 2022-2023

A nonno,
e agli occhi lucidi
che avrebbe avuto
sapendomi felice oggi.

Abstract

In the framework of the European project HITRI*plus* and the SIGRUM collaboration, the National Centre for Oncological Hadrontherapy (CNAO) has launched initiatives to design and build a superconducting gantry for hadrontherapy. Such a gantry is based on short and strongly bent superconducting dipoles that require an appropriate description of the quality of the produced magnetic field. In accelerator magnets, the field quality is conveniently described by a set of coefficients known as *field harmonics* or *multipole coefficients*. Generally, two different approaches can be used for determining the field harmonics. The first is the Fourier series expansion of a calculated field component along a circle. The second method provides an estimation of the field harmonics from the coefficients in a suitable Taylor series expansion in the case of symmetric fields. These methods are commonly used to analyse the field quality of long accelerator magnets with small apertures. However, in the case of such a gantry, a detailed investigation is required since the magnet is short and strongly curved with a relatively large gap. Moreover, the length of the coils' heads represents roughly 25% of the total length of the magnet thus the contribution of the introduced non-linear field components cannot be neglected. Both approaches were thoroughly examined in order to determine their applicability. The results revealed that the Fourier series expansion of the field components may not be appropriate for the field quality description of a magnet with a small bending radius. Indeed, the vector Laplace equation is not fulfilled due to the presence of an additional term and the interpretation of the coefficients results unclear. In the case of short and strongly bent magnets, the analysis method employed for determining the multipole coefficients considering a field symmetric about the median plane is the Taylor series expansion of the magnetic flux density. The multipole coefficients obtained through the Taylor expansion analysis were compared with the field components derived by particle tracking showing an agreement within a few units level. In conclusion, the field derivatives can be effectively used to represent short and strongly bent magnets in accelerator codes.

Contents

List of Figures

List of Tables

Chapter 1

Introduction

1.1 Hadrontherapy

Cancer appears to be one of the major causes of death and an important barrier to increasing life expectancy. In 2019, according to the World Health Organization (WHO), cancer is one of the leading cause of death before the age of 70 years in 112 of 183 countries. In 2020, worldwide, occurred an estimated 19 million new cancer cases and roughly 10 million cancer deaths. The global cancer cases are expected to be 28 million in 2040, a 47% rise from 2020. For global cancer control, preventive and therapeutic interventions are available for tumours and their integration into health planning nationally can serve to reduce the future incidence worldwide [1].

Radiotherapy, surgery and pharmacotherapy, such as chemotherapy and immunotherapy, are the principal methods for the treatment of oncological diseases. Up to 70% of cancer patients in developed countries receive radiotherapy alone or in combination with other methods. Proton and ion beam therapy is comparable in terms of cost with surgical treatment and 2.5 times less costly than pharmacotherapy of malignant tumors [2].

Particles such as protons, neutrons, nuclei of a few ions like carbon and oxygen belong to the class of hadrons, a Greek word meaning "strong", from which the word *hadrontherapy*, a form of radiotherapy for the treatment and cure of tumours, derives.

Globally, at the end of 2021, more than two hundred fifty thousand patients were treated with protons and heavy-ions [3] and a clear growth in terms of applications with respect to the early twenty-first century of this particle therapy can be noticed in Fig. 1.1.

As regards the charged hadrons in radiation therapy, the story started in 1945 when Ernest Lawrence asked his student to clarify the stopping process of protons in the matter. After some calculations, he realized that the depth profiles have a significant increase in dose at the end of their range in the matter, the so-called Bragg peak, and he wrote a paper on the possibility to concentrate the dose on the tumour target sparing healthy tissues better than what can be done with X-rays. This is considered the first work on hadron therapy [4].

For the record, the "dose" is the energy deposited per unit of mass in a body and is

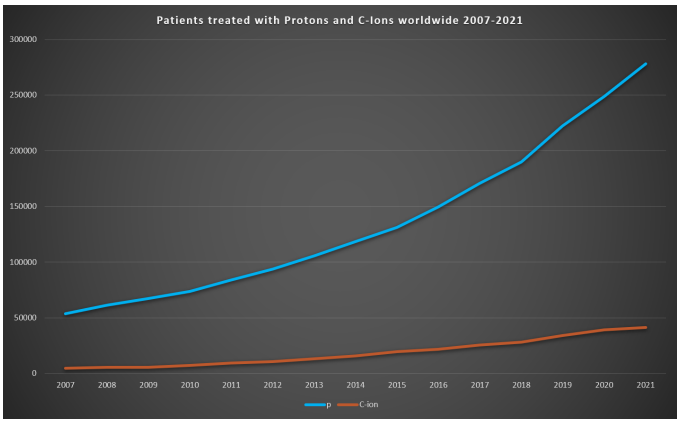

Figure 1.1: Statistics of patients treated in particle therapy facilities worldwide [3].

measured in Gray:

$$D = \frac{E\ [J]}{m\ [kg]} \tag{1.1}$$

where E is the energy deposited in a volume and m is the mass of the material volume.

The probability of causing cell damage increases with the dose but it is also necessary to keep safe the healthy tissues in the vicinity of the tumour. In that perspective, charged hadrons allow well-defined dose distribution in depth with respect to photons. Protons and carbon ions have, indeed, an energy distribution that guarantees low values of dose in the first part of the path inside a volume and a peak localized in the cancer zone, the Bragg peak previously cited, as shown in Fig. 1.2.

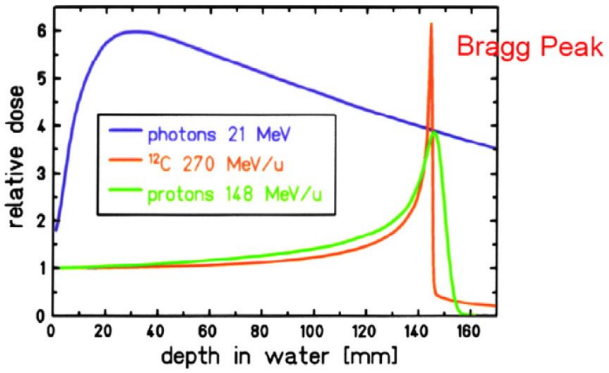

Figure 1.2: Depth dose distribution for photons, carbon ions and protons [5].

Within the hadron family, carbon ions have a silver lining compared to protons, i.e. the ability to transfer energy to matter over a path of equal length is more efficient and that implies more ionization acts over the same paths. To account for this effect, a parameter called *linear energy transfer* (LET) is introduced and it is defined as the density of energy deposition along the track of the particles within tissues measured in $keV\,\mu m^{-1}$.

In other words, densely ionizing radiation considerably reduces the possibility of repairing ionization damages allowing the overcoming of tumour radio-resistance, such as carbon ions that, in terms of cell destruction, are more efficient than protons as previously mentioned.

The property of particles related to higher or lower density of ionization acts is indicated as radiation quality measured in terms of *relative biological effectiveness* (RBE), i.e. the ratio between the photon and the ion doses necessary to produce the same biological effect. For instance, carbon ions give the maximum ratio of RBE in the Bragg peak which means that the irreparable damages are concentrated in that zone. In reality, some complications need to be added when one considers that the effects depend on many parameters not mentioned in this context such as cell type, blood perfusion and so on [6].

The noticeable advantages of hadrontherapy also require a careful cost analysis and a comparison with state-of-the-art photon radiotherapy techniques. Any advantage in terms of increased cure rate or reduction of acute and late complication rates results in cost savings for salvage treatments. Hadrontherapy centres are more complex and costly than conventional photon therapy units but the costs of radiotherapy in general, including hadrontherapy, are much lower than the costs of all other types of therapy for malignant diseases [7].

1.2 National Centre for Oncological Hadrontherapy (CNAO)

The status of hadrontherapy in the world shows a situation of strong expansion, with 105 operating centres as reported by the site of PTCOG, Particle Therapy co-operative Group (PTCOG), upated to October 2022 [3]. It should be remarked that some of these centres such as Pavia (Italy), Wiener Neustadt (Austria), Shanghai (China), Heidelberg and Marburg (Germany) and Hyogo (Japan) have accelerators which can accelerate both protons and carbon ions.

In Italy, the publication in 1991 of the report "For a centre of teletherapy with hadrons" by U. Amaldi and G. Tosi started the history of the National Centre for Oncological Hadrontherapy (CNAO). In 2014, CNAO started patient treatments within the national health system and it is the only Italian facility that operated with both protons and carbon ions to treat tumours. The centre is located in Pavia, in an area adjacent to other hospitals and to the city university campus, thus allowing for the creation of synergies and collaborations [8]. In 2020, an expansion project was approved with the aim of enlarging the number of possible tumour treatments and the number of patients in a year. In particular, CNAO will host a commercial proton therapy facility equipped with a rotating gantry and an accelerator-based Boron Neutron Capture Therapy (BNCT) [9].

From an engineering and physical point of view, the core of hadrontherapy at CNAO is the complex of accelerators and lines shown in Fig. 1.3a and Fig. 1.3b.

The particle accelerator is used to accelerate beams from 60 MeV to 227 MeV[1] for

[1]The maximum energy for clinical applications

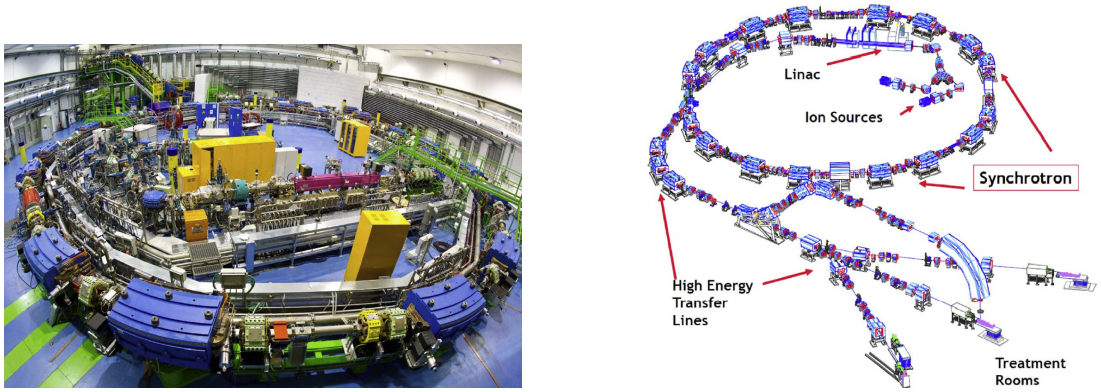

(a) (b)

Figure 1.3: (a) View of the synchrotron and beam transport lines [9]. (b) Layout of the high technology of CNAO [8].

protons and from 120 MeV/u up to 400 MeV/u[2] for carbon ions. Different energies are available to properly select the depth of the Bragg peak inside the body.

The dose distribution is "shaped" to surround the area to be treated exploiting a system called dose delivery. There are basically two categories of irradiation techniques: passive and active beam delivery. In the passive systems, the beam is first enlarged by scattering, then a variable thickness device degrades the energy to match the tumour depth. The energy spread is increased by employing a range modulator to obtain a *spread-out Bragg peak* (SOBP), the overlap of many Bragg peaks. The beam is then collimated to select the central uniform region and a multileaf collimator is employed to obtain the wanted shape. The passive dose delivery system is required to cover the tumour volume but unfortunately, an unwanted dose is delivered to the patient.

In the second technique, also called active scanning, a pencil beam is deflected by a couple of magnets and is used to "paint" an image. The target volume is subdivided longitudinally into iso-energetic "slices". Then, the beam energy is varied to treat each slice. With active scanning, the dose is distributed in small volumes called *voxels* (volume pixels) which are treated individually. The result is a better conformation of the dose and, consequently, the possibility to treat arbitrary tumour shapes. Active scanning requires that the position of the beam is controlled with high accuracy and therefore, also the target shape and position inside the body have to be precisely known. To treat tumours close to moving organs, e.g. the lungs, synchronization with breathing and other adjustments need to be implemented. In Fig. 1.4 the different conformation of the dose in the two delivery systems is approximately shown.

CNAO is designed for a fully active dose distribution system. The energy of the particles is varied by the synchrotron [8].

[2]Kinetic energy per nucleon

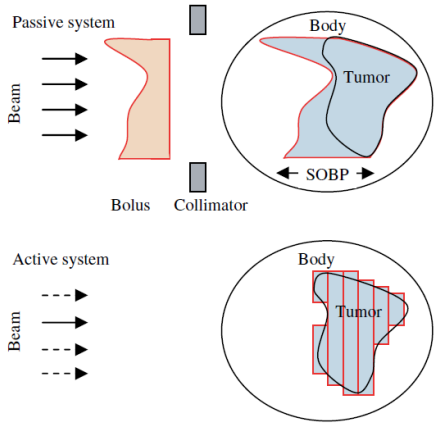

Figure 1.4: Conformation difference of the dose in passive and active systems. Healthy tissues are better spared with active beam delivery [6].

Once the particles have been accelerated, they are injected into beam-lines and transported into treatment rooms. The transfer lines can be either fixed or mobile, rotating around the patient. The latter solution is named *gantry* and allows irradiation from multiple directions. Thanks to the ability to select treatment angles, the dose to healthy tissues can be reduced and the treatment is less prone to delivery errors.

Currently, the presence of a proton gantry is widespread in hadron therapy centres while the gantries for carbon ions are limited to just few installations. The complexity of the technology and the high capital cost are the reason why the diffusion of this medical device is still limited.

1.3 Heavy-Ion Therapy Gantries

Gantries can be classified on the basis of the delivery system topology and its relative movement with respect to the patient [10]. The great majority of the gantries currently in operation are *isocentric* machines. The *isocenter* is defined as the point where the beam delivery direction crosses the tumour. A schematic representation of these gantry types is displayed in Fig. 1.5. If the rotation axis is not coincident with the patient location, the configuration of the gantry is called *ex-centric* but, in the present work, it has been chosen to use an isocentric configuration.

Theoretically, considering the case of full 360° rotation capacity of the gantry and a possible treatment table rotation of ±90°, the tumour can be irradiated from every point situated on a sphere around it, i.e. a "full 4π-irradiation" is realized. Nevertheless, geometrical constraints need to be observed to avoid collisions between patient and equipment [11].

On the one hand, the technology related to proton therapy gantries can be considered mature and nowadays several companies are able to commercialise specific solutions. On the other hand, carbon ions gantries are still in the early stage of their spread; however, it is clear that finding solutions with the aim of reducing size, weight and cost would

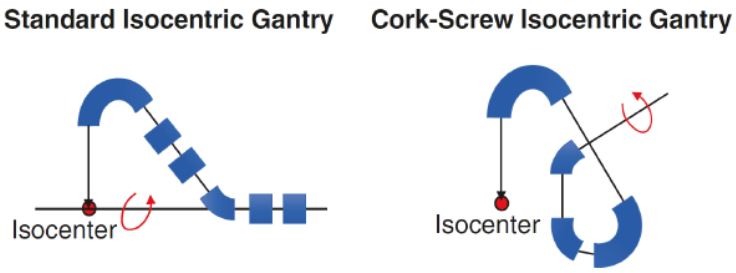

Figure 1.5: Schematic isocentric gantry layout types [10].

result in a significant diffusion of heavy-ions gantries. Examples of the latter gantries are described hereafter.

The Heidelberg Ion-beam Therapy centre (HIT, DE) is the first heavy-ion treatment facility with a gantry that has a rotation capacity of 360°. The rotating structure of the HIT gantry is installed on two large rings at both ends, the so-called *barrel* structure, as shown in Fig. 1.6. The total weight of rotating parts amounts to 570 tons and in addition there are 130 tons of room fixed components such as the main gantry supports. The energy range is between 50 and 430 MeV/u corresponding to a penetration depth in tissue between 20 and 300 mm. The first patient was treated with carbon ions in 2012 [12].

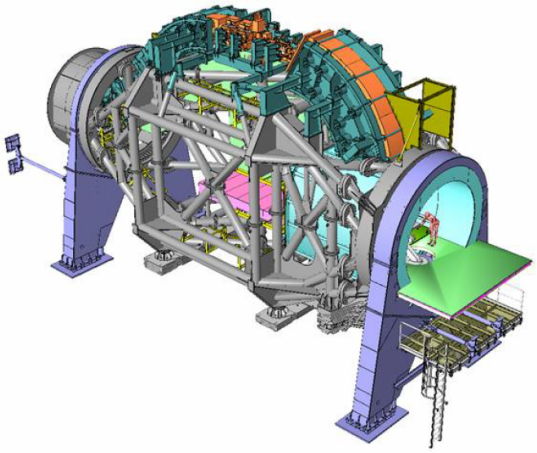

Figure 1.6: HIT isocentric ion gantry [13].

At the National Institute of Radiological Science (NIRS, JP), the carbon ions treatment has been carried out since 1994 using the Heavy-Ion Medical Accelerator in Chiba. The construction of a compact superconducting (SC) rotating-gantry was completed in the 2015 and in Fig. 1.7 is exhibit its three-dimensional picture. The gantry is designed to have a length approximately equal to 13 m and a beam orbit radius of 5.5 metres. The isocentric rotating gantry can deliver carbon ions with kinetic energy up to 430

MeV/u. The dimension of the facility is considerably reduced thanks to the presence of SC magnets in the beam-transport line, indeed the total weight is roughly 300 tons. Specifically, combined-function SC magnets with different apertures can provide both dipole and quadrupole fields avoiding the use of standard quadrupoles and allowing a relevant footprint reduction. The peak magnetic field is equal to 2.88 T and the maximum gradient is 9.3 T/m. The gantry is installed on a barrel structure and it can guarantee a full rotation within a range of ±180° [14] [10].

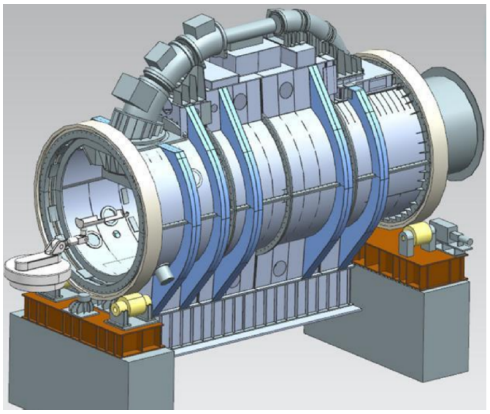

Figure 1.7: NIRS superconducting rotating gantry for heavy-ion therapy [10].

To achieve a further size reduction of the first SC gantry installed at NIRS, a next-generation SC rotating gantry has been developed in a project of the Yamagata University Hospital at the East Japan Heavy-Ion Centre. The same type of gantry will be also installed at the Yonsei University Health System and Seoul National University Hospital. A drawing of the magnet layout is shown in Fig. 1.8a. The maximum dipole and quadrupole field of the SC magnets is increased up to 3.5 T and, as a result, the gantry is downsized to 2/3 of the NIRS gantry, indeed the axial length is about 8 m and the radius is roughly 6 m. Another interesting aspect is the assembling of two types of quadrupole coils on the full surface of a single dipole coil as displayed in Fig. 1.8b. In order to excite the magnets separately, the dipole and quadrupole coils are electrically isolated and connected to an independent power supply. Moreover, the length of the scanning system is reduced by arranging a horizontal and a vertical scanning magnet in parallel to further reduce the dimensions of the machine; however, the level of complexity in the development of the scanning system is significantly higher [15].

1.4 The CNAO Gantry Project

In European context, an initiative launched by TERA (Foundation for oncological hadron therapy) and CERN (European Organization for Nuclear Research, Geneve) proposed a conceptual design of a very light (~50 tons, a factor 4 to 5 less than the present state-of-the-art) SC rotating gantry based on cosθ magnets called SIGRUM (Superconducting Ion Gantry with Riboni's Unconventional mechanics) [16]. After this pre-study phase,

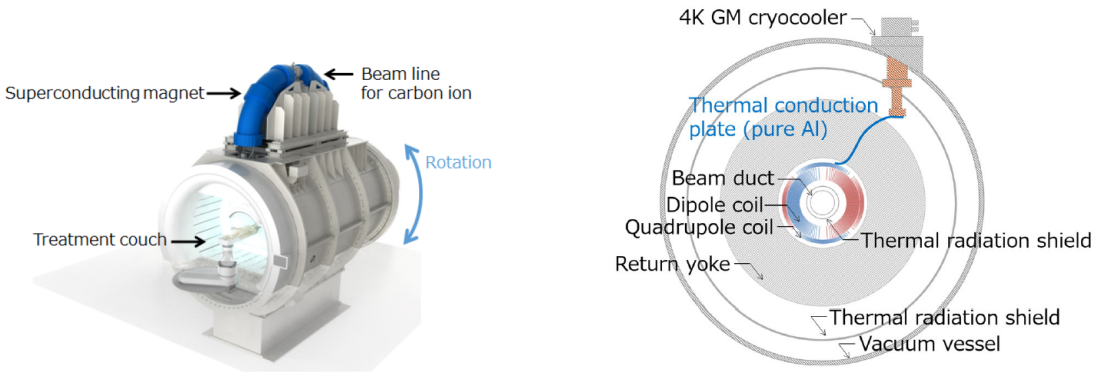

(a) (b)

Figure 1.8: (a) Compact superconducting gantry for carbon ion therapy [15]. (b) cross-section of the superconducting magnet [15].

the current collaboration among CERN, CNAO, MedAustron (centre for ion beam therapy and research located in Austria) and INFN (National Institute for Nuclear Physics, Italy), in the framework of both SIGRUM and HITRI*plus* (Heavy Ion Therapy Research Integration) projects, has resulted in a concrete first step toward the detailed design and construction of an evolution of the SIGRUM rotating gantry that might be implemented in the expansion project of CNAO Foundation. In Fig. 1.9 is represented a preliminary layout of the light SC rotating gantry [9].

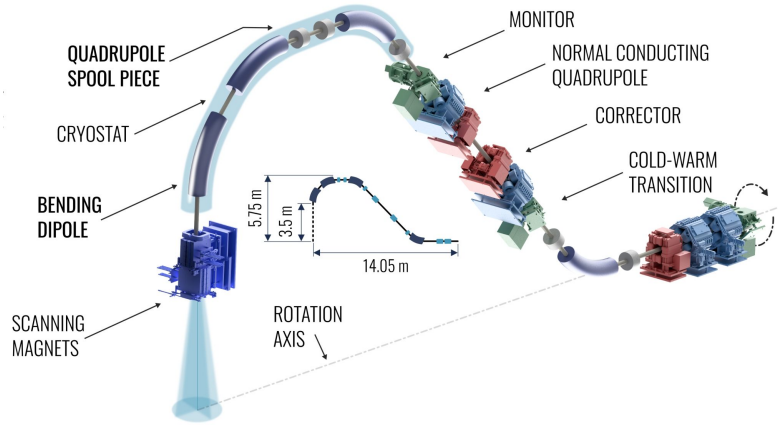

Figure 1.9: 3D layout of the superconducting ion gantry[9].

The construction of the entire facility will be preceded by an initiative called SIG (Superconducting Ion Gantry). The project foresees the construction of a 1 m long demonstrator to be manufactured and tested at INFN (LASA laboratory) in about three years with the aim of exploring the concrete possibility of using superconducting cosθ magnet technology. Specifically, the required field of the SC dipole magnets is equal to 4 T, the bore aperture is equal to 80 mm and the ramp rate is about 0.4 T/s. The required

field quality, in technical language, ranges from 1 to 10 units and it is reached typically in a region of about two-thirds of the magnet aperture. The most critical challenge is the curvature of the magnet, indeed a small bending radius between 1.3 and 1.6 m will be chosen dictated by the 430 MeV/u of C-ions which have a beam rigidity of $B\rho = 6.6$ Tm [17] [18].

It is important to underline that the demonstrator serves "only" to demonstrate that the main technical issues are solvable but this magnet is not directly employed in the SC rotating gantry for ion therapy planned in CNAO.

In conclusion, to compare the SIG demonstrator with other relevant SC dipoles employed in gantries and particle accelerators, a general overview is reported in Fig. 1.10 with the bending radius in abscissa and the squared product of field times the magnet aperture in ordinate. The latter parameter is related to the energy stored per unit length and it is proportional to the complexity of the magnet itself [18].

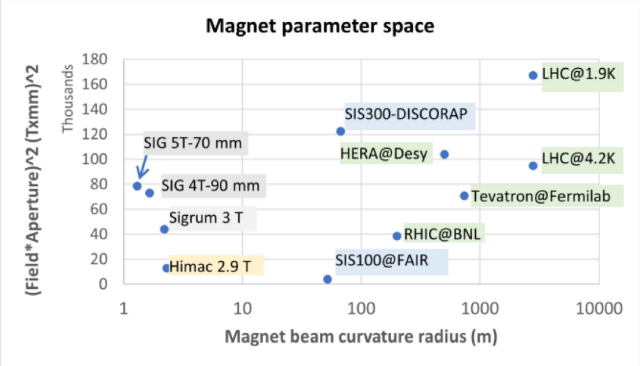

Figure 1.10: Plot of various magnets as a function of bending radius and the squared product of field times the magnet aperture [18].

Chapter 2

Field Quality Analysis

2.1 Field Harmonics in Straight Magnets

The field quality in accelerator magnets with a sufficiently large bending radius is generally described by a set of Fourier coefficients, also called field harmonics or multipole coefficients. The quality criteria of a magnetic field are assessed by defining limits on the unwanted multipole coefficients. The theoretical discussion presented here refers to [19]. The field harmonics are evaluated by finding a general solution with the separation of variables method that satisfies the Laplace equation, $\nabla^2 A_z = 0$ where A_z is the z-component of the magnetic vector potential. Considering $A_z = \rho(r)\phi(\varphi)$, the following equalities hold:

$$\frac{\partial A_z}{\partial r} = \frac{d\rho(r)}{dr}\phi(\varphi) \tag{2.1}$$

$$\frac{\partial^2 A_z}{\partial r^2} = \frac{d^2\rho(r)}{dr^2}\phi(\varphi) \tag{2.2}$$

$$\frac{\partial^2 A_z}{\partial^2 \varphi} = \frac{d^2\phi(\varphi)}{d\varphi^2}\rho(r) \tag{2.3}$$

Therefore, the Laplace equation in circular coordinates, a coordinate system commonly used for the computation of the field in long accelerator magnets, can be written as:

$$r^2\frac{\partial^2 A_z}{\partial r^2} + r\frac{\partial A_z}{\partial r} + \frac{\partial^2 A_z}{\partial \varphi^2} = 0 \tag{2.4}$$

After the introduction of a separation constant n^2, for the case $n \neq 0$, the solutions of two ordinary differential equations are obtained:

$$\rho_n(r) = E_n r^n + F_n r^{-n} \tag{2.5}$$

$$\phi_n(\varphi) = G_n \sin n\varphi + H_n \cos n\varphi \tag{2.6}$$

The vector potential is single-valued, thus it must be a periodic function in φ with $A_z(r,0) = A_z(r,2\pi)$. The separation constant n assumes integer values and the general solution of the homogeneous differential equation 2.4 is given by the following expression:

$$A_z(r,\varphi) = \sum_{n=1}^{\infty}(E_n r^n + F_n r^{-n})(G_n \sin n\varphi + H_n \cos n\varphi) \tag{2.7}$$

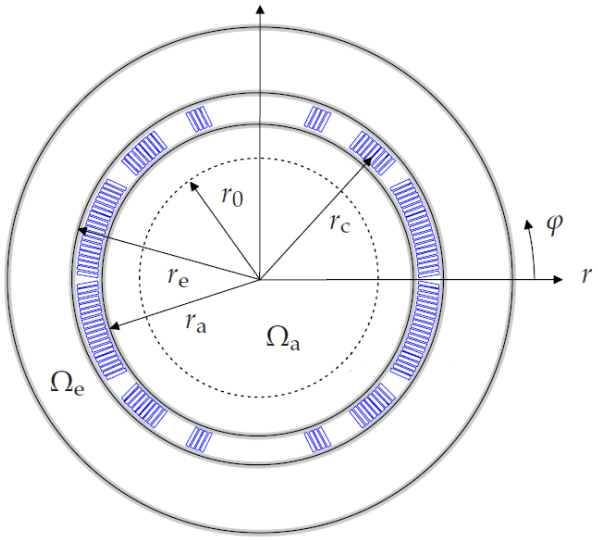

Figure 2.1: Representation of the aperture domain Ω_a and the exterior domain Ω_e in a 2D circular coordinates problem. The radius r_0 is the reference one at which the analysis is performed, φ is the angular position, r_a and r_e are respectively the aperture radius and the exterior one [19].

The aperture domain Ω_a (see Fig. 2.1) is considered the problem domain. The condition of a finite flux density at $r = 0$ imposes $F_n = 0$ and the introduction of two constants $C_n = E_n G_n$ and $D_n = -E_n H_n$ in Eq. 2.7 allows to evaluate the general solution for the vector potential in the selected domain:

$$A_z(r,\varphi) = \sum_{n=1}^{\infty} r^n (C_n \sin n\varphi - D_n \cos n\varphi) \tag{2.8}$$

The components of the field can be then expressed in the problem domain as:

$$B_r(r,\varphi) = \frac{1}{r}\frac{\partial A_z}{\partial \varphi} = \sum_{n=1}^{\infty} n r^{n-1}(C_n \cos n\varphi - D_n \sin n\varphi) \tag{2.9}$$

$$B_\varphi(r,\varphi) = -\frac{\partial A_z}{\partial r} = -\sum_{n=1}^{\infty} n r^{n-1}(C_n \sin n\varphi + D_n \cos n\varphi) \tag{2.10}$$

Each value of the integer n in the solution of the Laplace equation corresponds to a specific flux density distribution generated by an ideal magnet. For instance, n = 1,2,3 correspond respectively to the dipole, quadrupole and sextupole flux density distributions.

To determine the multipole coefficients or field harmonics C_n and D_n, two different approaches will be discussed.

The first method is a comparison of the integration constants in the general solution of the Laplace equation with the Fourier series expansion of the calculated field components along a circle. In the case of accelerator magnets, the domain is commonly chosen as a circle with a radius of 2/3 of the aperture radius. Imposing that the radial component of the magnetic flux density is calculated at a reference radius $r = r_0$ as a function of the angular position φ, the Fourier series expansion of the field components results in:

$$B_r(r_0,\varphi) = \sum_{n=1}^{\infty}(B_n(r_0)\sin n\varphi + A_n(r_0)\cos n\varphi \tag{2.11}$$

$$B_\varphi(r_0,\varphi) = \sum_{n=1}^{\infty}(B_n(r_0)\cos n\varphi - A_n(r_0)\sin n\varphi) \tag{2.12}$$

where

$$A_n(r_0) = \frac{1}{\pi}\int_0^{2\pi} B_r(r_0,\varphi)\cos n\varphi\, d\varphi \qquad n = 1,2,3... \tag{2.13}$$

$$B_n(r_0) = \frac{1}{\pi}\int_0^{2\pi} B_r(r_0,\varphi)\sin n\varphi\, d\varphi \qquad n = 1,2,3... \tag{2.14}$$

The components $B_n(r_0)$ and $A_n(r_0)$ are respectively named *normal* and *skew* multipole coefficients and are given in units of tesla at a reference radius r_0. It is common practice to normalize the coefficients with respect to the main field $B_N(r_0)$.

$$\begin{aligned} B_r(r_0,\varphi) &= \sum_{n=1}^{\infty}(B_n(r_0)\sin n\varphi + A_n(r_0)\cos n\varphi \\ &= B_N(r_0)\sum_{n=1}^{\infty}(b_n(r_0)\sin n\varphi + a_n(r_0)\cos n\varphi \end{aligned} \tag{2.15}$$

$$\begin{aligned} B_\varphi(r_0,\varphi) &= \sum_{n=1}^{\infty}(B_n(r_0)\cos n\varphi - A_n(r_0)\sin n\varphi) \\ &= B_N(r_0)\sum_{n=1}^{\infty}(b_n(r_0)\cos n\varphi - a_n(r_0)\sin n\varphi \end{aligned} \tag{2.16}$$

The small $b_n(r_0)$ and $a_n(r_0)$ are normal and skew multipole coefficients related to the main field $B_N(r_0)$[1].

[1] In this case, B_1 represents the dipole component, B_2 the quadrupole and so on.

The second method foresees a comparison of the field harmonics with the Taylor coefficients of a series expansion of the calculated flux density at the horizontal median plane. Assuming an up/down field symmetry, the skew multipole components can be assumed as null. Generally, the field can be expanded in the median plane $y = 0$ about an axis at x_0:

$$f(x) = \sum_{n=0}^{\infty} \frac{1}{n!}(x - x_0)^n f^n(x_0) = \sum_{n=0}^{\infty} \frac{1}{n!}(x - x_0)^n \frac{d^n f(x)}{dx^n}\bigg|_{x=x_0} \tag{2.17}$$

where f^n is the n-th derivative of the function at x_0. Since the transverse dimensions of the beam are small compared to the radius of curvature of the particle trajectory, the expansion can be performed in the vicinity of the reference trajectory [20]. Imposing $x_0 = 0$, the Eq. 2.17 is called Maclaurin series and the y-component of the magnetic flux density can be expanded on the median plane as:

$$B_y(x) = B_0 + \frac{dB_y}{dx}\bigg|_{x=y=0} x + \frac{1}{2!}\frac{d^2B_y}{dx^2}\bigg|_{x=y=0} x^2 + ... + \frac{1}{n!}\frac{d^nB_y}{dx^n}\bigg|_{x=y=0} x^n + ... \tag{2.18}$$

where the constant term B_0 corresponds to the dipole component, $\frac{dB_y}{dx}$ to the quadrupole one and so on.

To compare the results obtained with the two methods described, the relation between the multipole coefficients and the ones evaluated in the Maclaurin series can be derived:

$$b_n = \frac{r^{n-1}}{B_N}\frac{1}{(n-1)!}\frac{d^{n-1}B_y}{dx^{n-1}}\bigg|_{x=y=0} \tag{2.19}$$

where b_n represents the field unit component of order n, starting with $n = 1$ for the dipole, and B_N is the main field. Generally, to easily compare the values, the outcomes of the conversion formula Eq. 2.19 are multiplied by 10^4.

2.2 Field Harmonics in Curved Magnets

The application of a bending transformation to straight magnet conductors introduces unwanted field components in a magnet with a strong curvature. Generally, for large accelerators, the magnets can be approximated to be straight while compact accelerators require strongly curved magnets characterized by a small ratio of bending radius to aperture. The field quality in the body of a strongly curved magnet is described by a finite set of multipole coefficients, truncated to some order, which constitutes, in the 2D case, a full basis for the solution of the Laplace equation [21].

Nevertheless, considering the entire geometry of a strongly curved magnet, cylindrical multipoles in the transverse plane cannot describe the field because the introduced functions do not satisfy 2D Maxwell's equations. To characterize the transverse field in curved magnets, toroidal harmonics [22][23] are identified to describe appropriately the magnetic

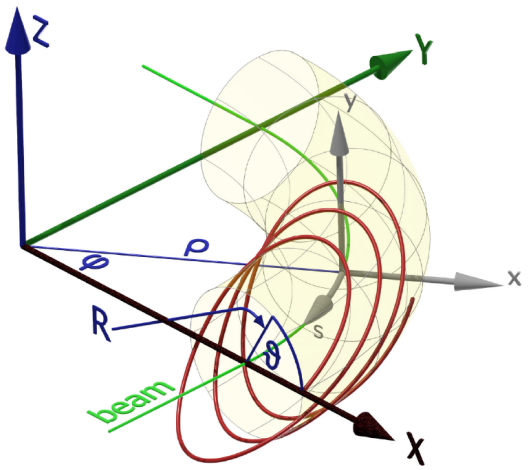

Figure 2.2: Representation of the coordinate system and variables for a curved magnet. The red line schematizes the winding geometry, the green line is the trajectory travelled by the particle beam, the capital X, Y, Z illustrate the global Cartesian coordinate system and the lower case x,y,s the beam one. The variables illustrated in the figure are the bending radius ρ, the angle around the beam ϑ, the magnet aperture radius R (or the winding radius) and the angle coordinate φ [21].

field but the topic will not be discussed in detail because for beam optics calculations is not practical to use directly the field expansion in terms of toroidal harmonics.

The magnetic field of a curved magnet cannot be described by any linear combination of the multipole coefficients previously discussed in Sec. 2.1. Indeed, by introducing a curved system shown in Fig. 2.2 with the bending radius ρ, invariance along the magnetic axis, and the transverse beam coordinates centred on the reference trajectory, the magnetic field can be derived from a vector potential which satisfies the following version of the Laplace equation in the current-free region [21]:

$$-\frac{\partial^2 A_z}{\partial x^2} - \frac{\partial^2 A_z}{\partial y^2} - \frac{1}{\rho + x}\frac{\partial A_z}{\partial x} + \frac{1}{(\rho + x)^2} A_z = 0 \tag{2.20}$$

The fact of the matter is that the definition of the multipole coefficients as the Fourier coefficients of the radial field on a reference circle around the nominal trajectory can still be possible but the interpretation of the results in a curved geometry is unclear. However, in this context, a correct characterization of the magnetic field in the transverse plane, assuming the presence of mid-plane symmetry, is possible by comparing the field harmonics with the coefficients of the Taylor series expansion [21].

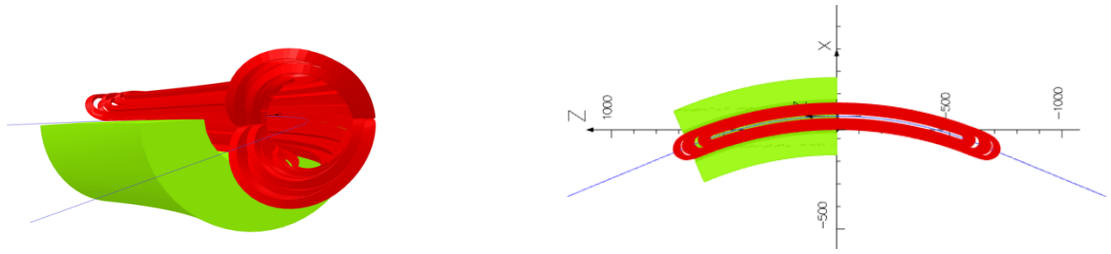

(a) (b)

Figure 2.3: (a) 3D representation of the magnetic coils in red and the iron yoke in green. (b) View of the magnet in the plane XZ. In both figures, the trajectory of the reference particle is shown in blue.

2.3 Description of the Magnet Model

The magnet model considered in the evaluation of the field harmonics is based on 45° 4T superconducting dipoles (with an aperture of 80 mm), shown in Fig. 2.2. The 2D cross-section of the magnet is optimized to be a pure dipole and the curvature of the magnet introduces an additional quadrupolar component and it can be considered as a combined function magnet. In general, the *combined function* magnets combine the dipole field for the deflection of the particles and the quadrupole field for focusing the particle beam in one plane and for defocusing in the other plane [24].

The bending of the particles on the XZ plane occurs thanks to the action of the y-component of the magnetic field. As shown in Fig. 2.4, the y-component of the field decreases rapidly after passing the heads of the dipole. The clinical requirement for carbon ions of a maximum kinetic energy of 430 MeV per nucleon, corresponds to a beam rigidity of 6.6 Tm. This results in a radius of curvature ρ of 1.65 m and a total length l of about 1.3 m [25] [18]. The total length of the field map used is roughly 1.78 m and this ensures that the field components at the end of the magnetic field map are roughly null. In this design, the heads account for approximately 25% of the total length of the magnet and the field transition to zero cannot be approximated as a hard edge model [10]. The strong contribution of the heads generates non-linear components of the magnetic field that cannot be neglected. The sections below describe in detail the field quality analysis performed with the two analysis methods previously introduced, i.e. the comparison of the field components with the Taylor coefficients and the Fourier series expansion, considering a 3D magnetic field map generated from the Opera Simulation Software [26]. Then, the data of the 3D magnetic field map are interpolated with cubic interpolation in order to obtain the values of the magnetic field at the desired coordinates.

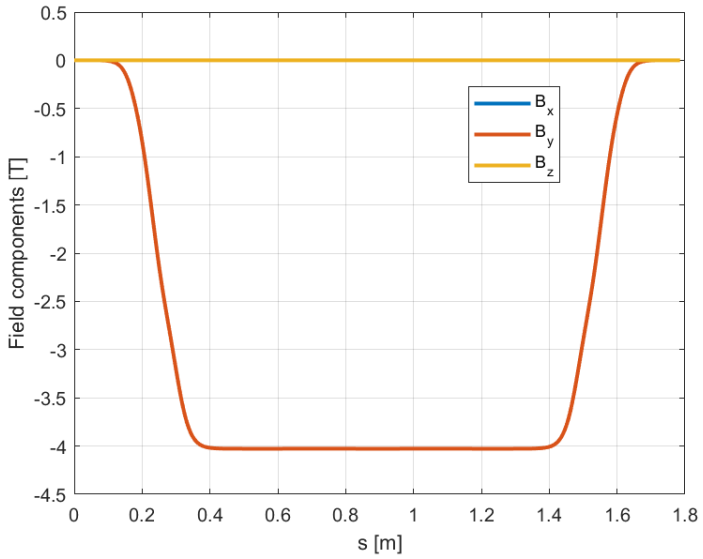

Figure 2.4: Representation of the behaviour of the magnetic field components in tesla plotted with respect to the reference particle trajectory.

Chapter 3

Taylor Series Expansion

3.1 Trajectory Analysis

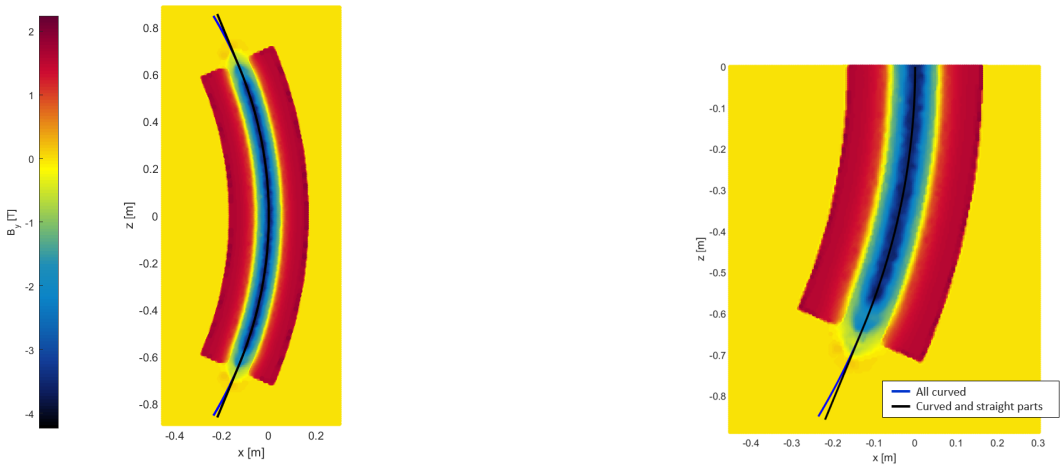

(a) (b)

Figure 3.1: (a) Illustration of the magnetic field map where the colour bar on the left represents the values of the y-component of the magnetic field; the blue curve is the all-curved trajectory of the reference particle and the black one is curved up to $\pm 22.5°$ and then straight to simulate the drift length. (b) Zoom on the discrepancy between the two particle trajectories studied for the analysis.

To properly represent the orbit of the reference or ideal particle, defined as the particle that follows the nominal geometry of the magnet and that is deflected by the nominal bending angle of 45°, two different approximated trajectories were analyzed and illustrated in Fig. 3.1a and Fig. 3.1b. The first trajectory is the simplified one in fact it considers only an arc of a circle with a radius of curvature ρ and the variable φ ranging from $-31°$ to $31°$. This specific range covers the total length of 1.78 m and it assures that the field components at the end of the field map are roughly null. The second trajectory is

constructed considering an arc of a circle with the same radius of curvature ρ, φ ranging from $-22.5°$ to $22.5°$ and two straight parts from the end of the arc to the end of the map. The parameter l_d, representing the drift length, is about 0.24 m for each straight part. A "drift" in the jargon of accelerators is a field-free region [20].

As can be noticed in Fig. 3.1b, the two trajectories differ in the drift region. Analyzing the field along different paths yields different results, especially for the coefficients represented by the odd derivatives, but the entire field quality analysis is not irremediably compromised by the selection of one of the two trajectories.

The choice of the trajectory constituted by the arc of a circle and the two straight parts is clearly visible in Fig. 3.2 where the black curve, the one representative of the previously mentioned trajectory, is the better approximation of the reference particle trajectory, the red dashed curve, simulated by the particle tracking tool, a MatLab algorithm implemented to perform the local tracking inside the 3D magnetic field map of the magnet, also described in [27]. The values of the magnetic field are visible in Fig. 3.1a where the field component is represented in a 2D plot.

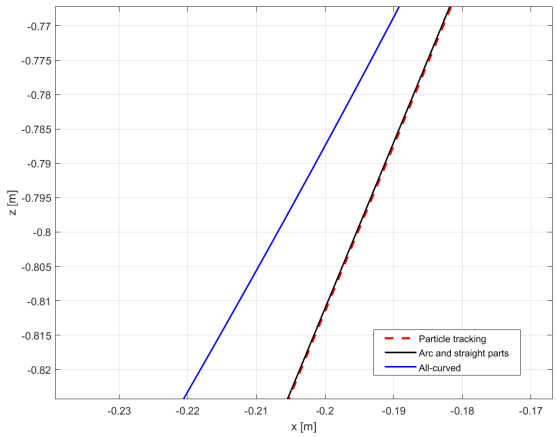

Figure 3.2: The blue curve represents the circular trajectory with φ ranging from $-31°$ to $31°$, the black curve is the combination of an arc of a circle with $-22.5° \leq \varphi \leq 22.5°$ and two straight parts and, finally, the red dashed curve corresponds to the reference particle trajectory evaluated with the particle tracking.

3.2 Taylor Series Expansion Analysis

With the purpose of analyzing the field quality of the curved dipole described in Sec. 2.2, the first step is the evaluation of the y-component of the magnetic flux density B_y. The last-mentioned flux density can be expanded as Eq. 2.18 on the median plane after imposing $x_0 = 0$. As discussed above in Sec. 3.1, the reference particle trajectory in the bending plane is assumed to be the reference path s on which a set of perpendicular segments, represents in Fig. 3.3, is defined and therefore B_y is assessed on each segment. The half-length of each segment ΔL is equal to 21.6 mm. Specifically, ΔL is selected to

be inside a region in which, as a first approximation, the magnetic field behaves properly (in the case of accelerator magnets, this region is conventionally defined as two-thirds of the aperture radius) and to be coherent with the particle beam size employed in the particle tracking tool to benchmark the field components obtained through the Taylor analysis of the magnetic field map [27].

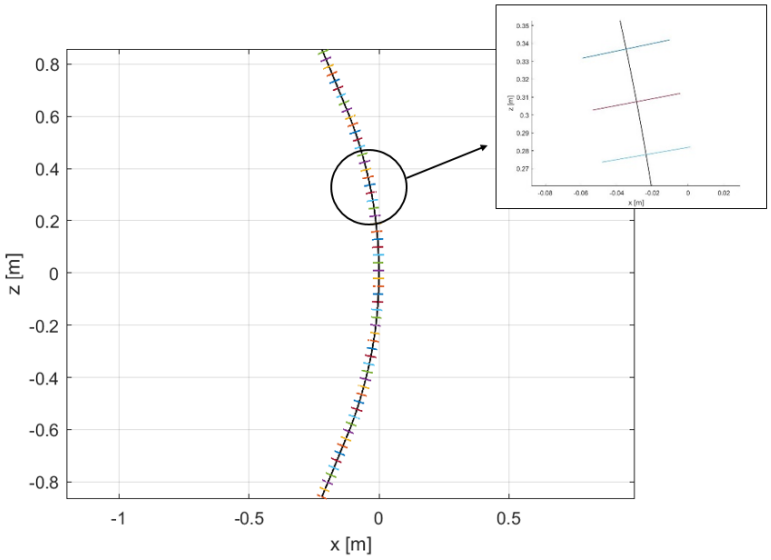

Figure 3.3: Representation of the reference trajectory s on which a set of perpendicular segments is defined.

The interpolation of the y-component of the magnetic field B_y with respect to the local x-coordinate identified on the segment itself is calculated using a polynomial curve fit *polyfit* in MatLab. Basically, the MatLab function polyfit is employed to evaluate the coefficients for a polynomial $p(x)$ of a degree n, defined as $p(x) = p_1 x^n + p_2 x^{n-1} + ... + p_n x + p_{n+1}$, that is the best fit for the data in y. The data in x are defined as the query points and the data in y are the fitted values at query points. Specifically, the query points are the points identified on the segments perpendicular to the reference trajectory and the data in y are the values obtained by the function that performs the interpolation on a 3D data set represented by the magnetic field map values from the Opera Simulation Software. The number of points set on the perpendicular segment is equal to 200 in order to guarantee a sufficiently accurate analysis. The match between the y-component of the magnetic flux density and the interpolated curve obtained with the polynomial curve fit in MatLab is represented in Fig. 3.4a where, as an example, it is illustrated the behaviour of B_y and the polynomial curve in a segment positioned in the body of the dipole, indeed the values of the magnetic field reported on the vertical y-axis are roughly equal to 4 T, i.e. the required dipole field. As a comparison, it is also illustrated an overlap between the flux density and the interpolated curve in the case of the length of the segment ΔL is set equal to 33 mm, a greater value than the one identified considering the two-thirds

of the aperture radius (see Fig. 3.4b).

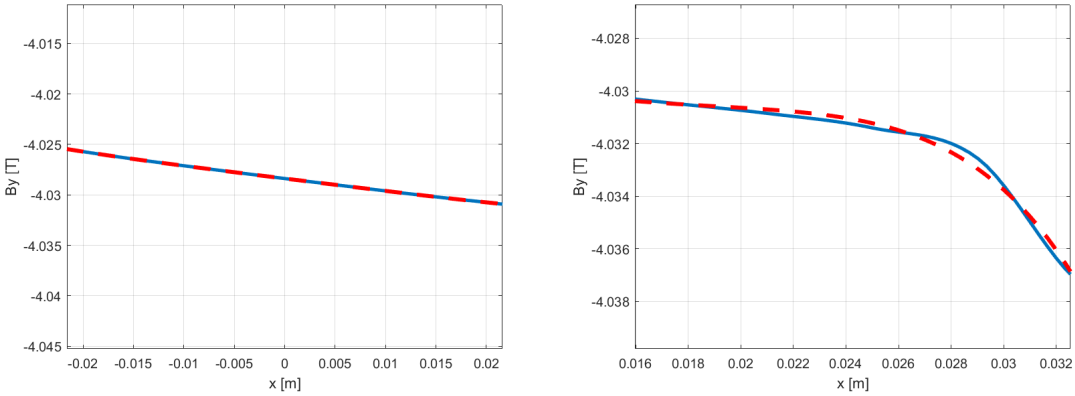

(a) (b)

Figure 3.4: (a) Representation of the y-component of the magnetic flux density B_y in blue and the interpolated curve obtained with the polynomial curve fit in red considering $\Delta L = 21.6$ mm. (b) Representation of the B_y in blue and the interpolated curve in red considering $\Delta L = 33$ mm. In both figures, the x-axis represents the points located on the segment with a half-length ΔL and the y-axis shows the values of the field of a segment placed around the middle of the reference trajectory.

The coefficients assessed by the interpolation are then multiplied by the factorial of $(n-1)$, where n is the degree of the polynomial term, in order to define the multipole coefficients of the field B_y on each segment along the reference trajectory. Specifically, the polynomial coefficients p_0, p_1, p_2, p_4 are associated with the field components introduced in Eq. 2.18 shown again here:

$$B_y(x) = B_0 + \left.\frac{dB_y}{dx}\right|_{x=y=0} x + \frac{1}{2!}\left.\frac{d^2B_y}{dx^2}\right|_{x=y=0} x^2 + \frac{1}{3!}\left.\frac{d^3B_y}{dx^3}\right|_{x=y=0} x^3 + \frac{1}{4!}\left.\frac{d^4B_y}{dx^4}\right|_{x=y=0} x^4$$

The equality between the polynomial coefficients and the field derivatives up to the decapole component identified with $n = 4$ is explicitly reported in Eq. 3.1:

$$\begin{aligned} B_0 &= p_0 \\ \frac{dB_y}{dx} &= p_1 \\ \frac{d^2B_y}{dx^2} &= 2!\ p_2 \\ \frac{d^3B_y}{dx^3} &= 3!\ p_3 \\ \frac{d^4B_y}{dx^4} &= 4!\ p_4 \end{aligned} \tag{3.1}$$

In Fig. 3.5, the behaviour of the field components along the trajectory of the reference particle s is illustrated. Generally, the polynomial degree is established according to the multipole coefficients which are to be analyzed. In Appendix A, a detailed polynomial convergence analysis is described in order to demonstrate that the multipole coefficients after the decapole are negligible.

The dipole component, i.e. the main field component shown in Fig. 3.5a, assumes the value of 4 T in the body of the magnet and decreases rapidly in the magnet heads down to 0 T in the field-free region. In the plot of the quadrupole component is clearly visible the connection point between the arc of a circle and the two straight lines which correspond to the points identified at $\pm 22.5°$. However, the geometric approximation introduced does not interfere with the results. The other even derivatives that represent the sextupole and the decapole field components indicate a lower fluctuation tendency with respect to the odd-derivatives, as the octupole component.

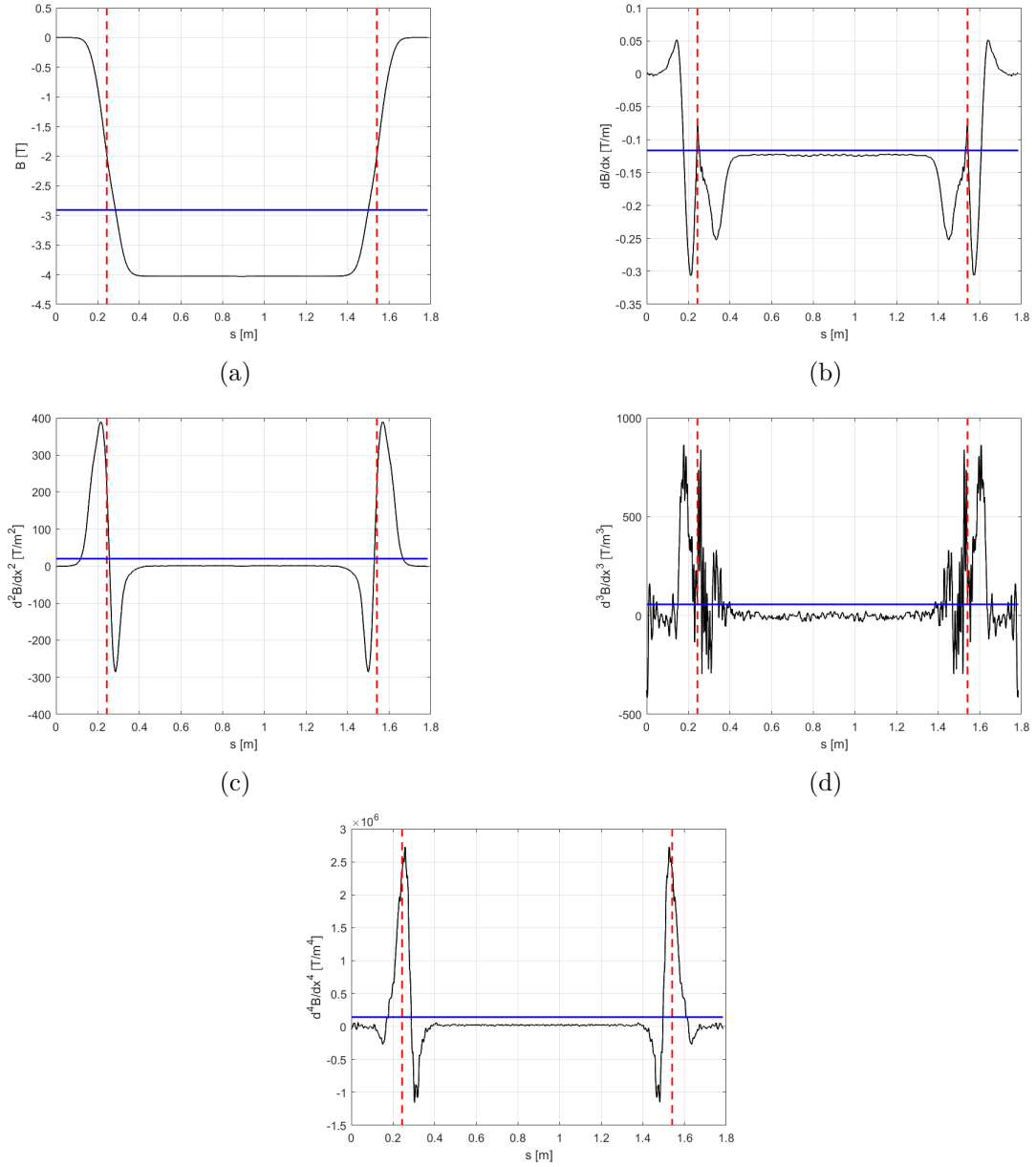

Figure 3.5: (a) The dipole component plotted along the reference trajectory. (b) The quadrupole component plotted along the reference trajectory. (c) The sextupole component plotted along the reference trajectory. (d) The octupole component plotted along the reference trajectory. (e) The decapole component plotted along the reference trajectory. In all figures, the dashed lines in red indicate the points at $\pm 22.5°$ that represent the range of the angle φ considering a reference trajectory constructed with an arc of a circle and two straight parts and the blue line represents the values of the average integral calculated by normalizing the integral results for the reference trajectory path.

3.3 The Integral of the Taylor Series Expansion Coefficients

To retrieve the values of the n-poles components for the complete magnet, the integral of the multipole components is approximated as follows:

$$\int_0^s \frac{d^{n-1}B_y}{dx^{n-1}} ds \approx \sum_{i=1}^{N-1} \frac{d^{n-1}B_{y,i}}{dx_i^{n-1}} \Delta s_i \tag{3.2}$$

where s represents the length of the reference trajectory travelled by the ideal particle; N is the total number of points established along the entire path s with the aim of assuring a fair approximation of the integral operation and therefore i ranges from 1 to $N-1$; Δs_i is the discrete step-length.

Integral of Taylor coefficients				
Dipole	**Quadrupole**	**Sextupole**	**Octupole**	**Decapole**
$[Tm]$	$[T/m\ m]$	$[T/m^2\ m]$	$[T/m^3\ m]$	$[T/m^4\ m]$
-5.19	-0.21	36.20	101.43	2.57×10^5

Table 3.1: Results obtained by the integral of the multipole coefficients evaluated with Eq. 3.2.

Then, the average integral is calculated normalizing the results retrieved from Eq. 3.2 by the length of the reference trajectory s traveled by the ideal particle and the values obtained are shown in Tab. 3.2. The bending of the magnet coils introduces a quadrupole gradient equal to 0.12 T/m in the horizontal plane in addition to the weak focusing effect which is compatible with the beam optics and does not have to be compensated [25]. The results of the average integral are illustrated in Fig. 3.5 with the blue lines.

Average integral of Taylor coefficients				
Dipole	**Quadrupole**	**Sextupole**	**Octupole**	**Decapole**
$[T]$	$[T/m]$	$[T/m^2]$	$[T/m^3]$	$[T/m^4]$
-2.91	-0.12	20.27	56.81	1.44×10^5

Table 3.2: Results obtained by the average integral of the multipole coefficients. The normalization is performed by considering the length of the entire reference trajectory travelled by the ideal particle.

To convert the outcomes in field units, the conversion formula Eq. 2.19 is used at $r = r_0$ equal to 21.6 mm. The field units are commonly used by the magnet design community to easily compare the evaluated results and to determine whether the outcomes are technically acceptable. Specifically, the results indicated in Tab. 3.1 are the ones converted in the mentioned above equation. The values in field units are displayed in Tab. 3.3. In this case, the value of B_N, i.e. the integrated dipole field, is calculated with the relation Eq. 3.2 and is equal to -5.19 Tm.

Multipole coefficients in field units				
Dipole [-]	**Quadrupole [-]**	**Sextupole [-]**	**Octupole [-]**	**Decapole [-]**
10000	8.65	-16.26	-0.33	-4.48

Table 3.3: The values of the multipole coefficients converted in field units using the conversion formula Eq. 2.19 where $r = r_0$ is equal to 21.6 mm. The main field B_N employed in the formula is the value of the integrated dipole component.

The sign of the multipole coefficients converted in field units is not relevant for evaluating the acceptability of the outcomes. Concerning the quadrupole field component, the imposed limit of around 10 units to guarantee uniformity in the good field region is respected while the sextupole component is slightly above the range. The latter field component requires further optimization to reach the acceptable limit. The other high-order multipole coefficients present satisfactory results for analysis purposes.

3.4 The Taylor Series Expansion Coefficients of the Integrated Field

To approximate the field harmonics from the coefficients of a Taylor series expansion, a different configuration is involved in the analysis. Instead of performing the integral of the multipole components considering the reference trajectory s of the ideal particle, it is reasonable to integrate and normalize the y-component of the magnetic flux density introducing the so-called toroidal lines illustrated in Fig. 3.6.

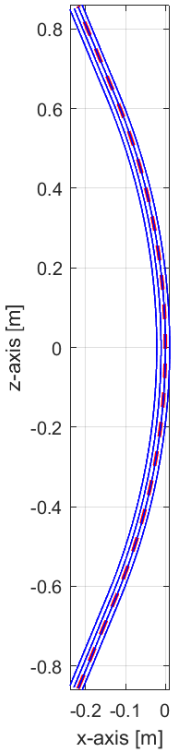

Figure 3.6: The curves in blue are the representation of the toroidal lines and the dashed curve in red is the illustration of the reference particle trajectory.

The integral and the normalization of the magnetic field B_y are evaluated in order to obtain the segment representing the local x-coordinate on which the interpolation with a MatLab polynomial curve fit is performed. The values of the normalized magnetic field are reported on the colour bar in tesla and the range is coherent with the value of the average integral of the dipole component illustrated in Tab. 3.2. The normalization of the integrated magnetic field is calculated considering the length of each toroidal line and it is useful to take into account the different path lengths of the toroidal lines. As mentioned, the interpolation is evaluated with the MatLab function *polyfit* generated with the least square method. In this case, the query points are the points identified on the segment representing the local x-coordinate and the y data are the values calculated by integrating

and normalizing the y-component of the magnetic field. The match between the integrated and normalized y-component of the magnetic flux density and the interpolated curve obtained with the polynomial curve fit is represented in Fig. 3.7. The behaviour of the integrated and normalized magnetic field B_y and the polynomial curve exhibits a shifted parabola which is the result of the non-negligible presence of the quadrupole and sextupole field components.

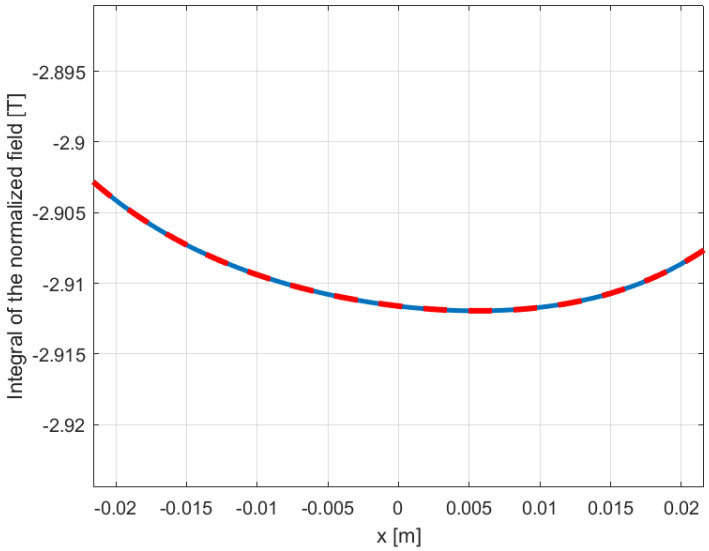

Figure 3.7: Illustration of the trend of the integrated and normalized magnetic field in blue and the behaviour of the interpolated curve obtained with the polynomial curve fit in red. The x-axis shows the values of the points identified on the segment and the y-axis represents the values of the integrated and normalized field.

Therefore, the results calculated by interpolating the data with the MatLab polynomial curve fit are multiplied by the factorial of $n-1$ as shown in Eq. 3.1, where n is the degree of the polynomial term, in order to define the multipole coefficients of the integrated and normalized field B_y on the horizontal segment.

The field components are then reported in Tab. 3.4.

Taylor coefficients of the integrated and normalized field				
Dipole $[T]$	**Quadrupole** $[T/m]$	**Sextupole** $[T/m^2]$	**Octupole** $[T/m^3]$	**Decapole** $[T/m^4]$
-2.91	-0.12	20.21	57.00	1.44×10^5

Table 3.4: Field components obtained after the interpolation of the data calculated by integrating and normalizing the y-component of the magnetic field.

The results shown in Tab. 3.4 are converted in field units exploiting the conversion formula Eq. 2.19. In this case, the main field component B_N is the dipole field component

calculated considering the integrated and normalized magnetic field B_y and its value is equal to -2.91 T. The values of the multipole coefficients converted in field units are reported in Tab. 3.5.

Multipole coefficients in field units				
Dipole [-]	**Quadrupole [-]**	**Sextupole [-]**	**Octupole [-]**	**Decapole [-]**
10000	8.64	-16.19	-0.33	-4.48

Table 3.5: The values of the multipole coefficients converted in field units using the conversion formula Eq. 2.19. The main field B_N employed in the formula is the value of the integrated and normalized dipole component.

The results converted in field units are similar to the ones evaluated in Tab. 3.3. Once again, it may be underlined that the sextupole field component requires an improvement in order to guarantee the demanded limit of 10 units.

To demonstrate that the two analysis approaches are consistent with each other, a comparison between the values of the retrieved field components is performed. Specifically, the difference in absolute value of the multipole coefficients converted in field units and reported in Tab. 3.3 and Tab. 3.5 is calculated. The results are shown in Tab. 3.6 and all the differences are below 0.1 field units. The dipole difference is perfectly equal to zero because the multipole coefficients expressed in field units are normalized with respect to the value of the main field B_N, therefore no relevant information is added by reporting the dipole difference.

Difference in absolute value				
Dipole [-]	**Quadrupole [-]**	**Sextupole [-]**	**Octupole [-]**	**Decapole [-]**
0	0.0021	0.0667	0.0007	0.0051

Table 3.6: The difference in absolute value of the multipole coefficients retrieved by the two different approaches and expressed in field units. In particular, the difference is performed between the values reported in Tab. 3.3 and in Tab. 3.5.

3.5 Trajectory from the Particle Tracking Tool

Before proceeding into further details of the field quality analysis, it may be useful to remind a few concepts of particle physics. The total energy of a particle is the sum of its rest energy $E_0 = mc^2$, where m and c are respectively the particle mass and the speed of light, and the kinetic energy K [28]:

$$E_{tot} = E_0 + K \tag{3.3}$$

To change the depth of the Bragg peak in a given material, the kinetic energy of the particles has to be modified. For instance, considering the energy range of carbon ions

from 120 MeV/u up to 430 MeV/u, the penetration depth in water ranges from 3 to 30 cm in order to reach deep tumour location [11]. The Lorentz factor γ_L is given by:

$$\gamma_L = \frac{E_{tot}}{E_0} \tag{3.4}$$

Therefore, the velocity of the particle can be calculated as follow:

$$v = c\sqrt{1 - \frac{1}{\gamma_L^2}} \tag{3.5}$$

The momentum $p = \gamma_L m v$ can be expressed as:

$$p = \frac{1}{c}\sqrt{E_{tot}^2 - E_0^2} \tag{3.6}$$

The beam rigidity $B\rho$ is defined as the ratio between the particle momentum p and the particle charge q:

$$B\rho = \frac{p}{q} \tag{3.7}$$

This quantity is expressed in Tm and indicates how the particles interact with an applied magnetic field or, in other words, how *rigid* is the beam in relation to the bending force introduced by the magnetic field. The beam rigidity for carbon ions of 430 MeV/u is $B\rho = 6.6$ Tm. The motion of a charged particle subjected to a magnetic field is governed by the Lorentz force:

$$F_L = \gamma_L m \frac{d\mathbf{v}}{dt} = q(\mathbf{v} \times \mathbf{B}) \tag{3.8}$$

where $\mathbf{v}$ and $\mathbf{B}$ are respectively the particle velocity and the magnetic flux density. The solution of Eq. 3.8 determines uniquely the particle trajectory in vacuum. Considering a circular orbit, a centripetal force can be introduced:

$$F_c = \frac{\gamma_L m v^2}{\rho} \tag{3.9}$$

Considering the Eq. 3.8 for a one-dimensional transverse flux density and combining it with Eq. 3.9, the definition of beam rigidity $B\rho$ can be derived as reported in Eq. 3.10:

$$B\rho = \frac{\gamma_L m v}{q} = \frac{p}{q} \tag{3.10}$$

Taking into account that the beam rigidity corresponds to $B\rho$ =6.6 Tm and the magnetic field B is equal to 4 T, the radius of curvature ρ results equal to 1.65 m.

To analyse the transport of the particle beam and specifically, the transport of the ideal particle for the purpose of the field quality analysis, a particle tracking tool implemented in MatLab is introduced to perform the tracking inside the 3D magnetic field map illustrated in Fig. 3.1a. The tracking algorithm is employed to produce the trajectory of the reference particle without geometric approximation as a circle and straight lines. The 3D magnetic field map is calculated with Opera Simulation Software and then it is interpolated in MatLab in order to properly describe the magnet. The MatLab function

ode45 [29] is used in the tracking algorithm to propagate the particle in the magnet. The function is based on the Runge-Kutta-Fehlberg method useful for the numerical solution of ordinary differential equations (ODE). Thanks to the function ode45, the Lorentz force is integrated and divided by the relativistic mass of the particle in order to obtain the velocity of the particle at different instants:

$$\int_{T_{i-1}}^{T_i} \frac{d\mathbf{v}(t)}{dt}\, dt = \int_{T_{i-1}}^{T_i} \frac{q}{m\gamma}(\mathbf{v}(t) \times \mathbf{B})\, dt, i = 1, ..., n \tag{3.11}$$

where q is the particle charge, m and v are respectively the mass and the velocity of the particle, γ is the relativistic Lorentz factor. The relative error tolerance in the particle tracking is set equal to 10^{-9}. The detailed description of the particle tracking algorithm is reported in [30], [27] and a similar approach is also implemented in [31]. The entire path followed by the ideal particle and evaluated by exploiting the particle tracking tool is illustrated in Fig. 3.8. The green line is the representation of the reference particle trajectory in the whole magnet. The nominal orbit of a carbon ion particle with an energy equal to 428 MeV/u is determined by setting an entry angle of 22.5°, which coincides with the exit angle of the particle, at the entrance of the dipole. It is more convenient to fine tune the beam energy to get the nominal deflection angle in the current field map than running the Finite Element Analysis for fine tuning the magnet current to deflect the nominal beam by the nominal angle. However, the magnetic field still needs to be optimized to guarantee the same exit angle at 430 MeV per nucleon which is the nominal energy of the gantry.

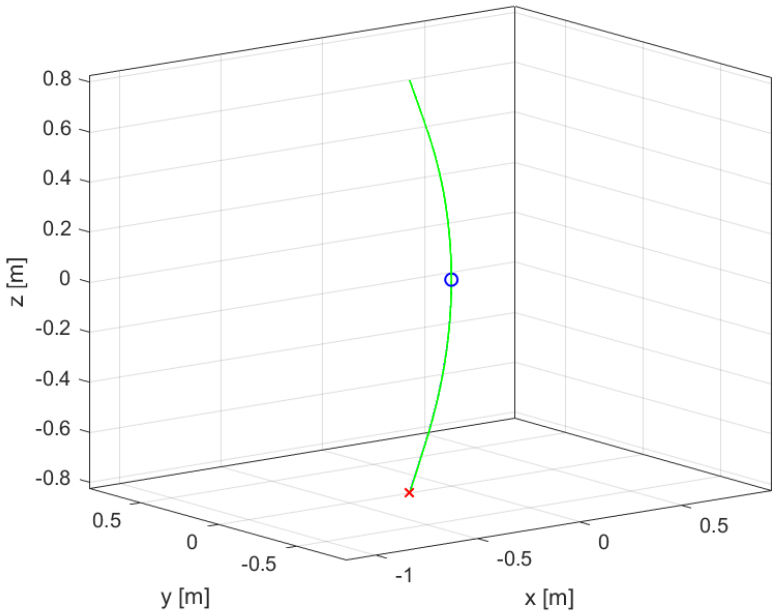

Figure 3.8: Representation of the entire reference particle trajectory (green line).

After the evaluation of the particle trajectory exploiting the particle tracking tool, the

coefficients of the Taylor series expansion are assessed. First of all, a set of equally-spaced segments is defined perpendicularly to the reference trajectory of the ideal particle and it is illustrated in Fig. 3.9.

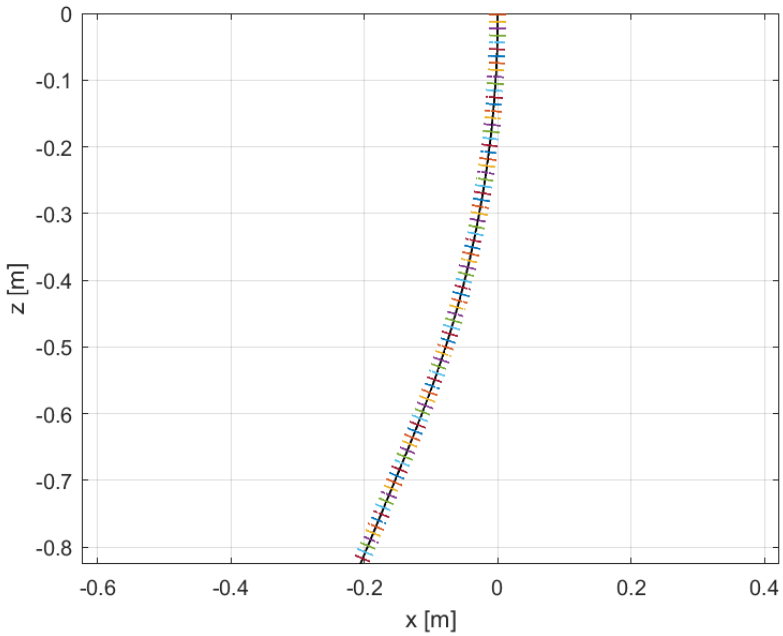

Figure 3.9: Representation of a set of segments equally paced and constructed perpendicularly to the reference particle trajectory.

To calculate the field components, the polynomial curve fit generated with the least square method, the MatLab function *polyfit*, is employed to perform the interpolation of the y-component of the magnetic field B_y with respect to the local x-axis identified by each segment. Also in the case of the trajectory determined with the tracking particle tool, the half-length of each segment ΔL is selected to be equal to 21.6 mm in order to assure the comparability of the results. Thus, the coefficients of the polynomial $p(x)$ assessed by the interpolation function are then multiplied by the factorial of $(n-1)$, where n is the degree of the polynomial term, in order to calculate the multipole coefficients of the field B_y on each segment as shown in Eq. 3.1.

The behaviour of the field components along the tracked reference particle trajectory is represented in Fig. 3.10. The trends of the dipole and the sextupole components are really close to the ones illustrated in Fig. 3.5a and Fig. 3.5c. The behaviour of the quadrupole field component evaluated by considering the tracked reference trajectory does not identify the junction points as a consequence of the geometric approximation of the particle trajectory with an arc of a circle and two straight parts clearly visible in Fig. 3.5b. In the case of the tracked trajectory, the same area appears more smooth. To clarify, the junction points cannot be identified on any of the figures due to the different evaluation of the trajectory then, in all field components graphs, the junction point zone is characterized by a greater regularity. The octupole and the decapole components are

the ones that show larger differences with respect to the other plots displayed in Fig. 3.5, indeed Fig. 3.5d and Fig. 3.5e have more pronounced fluctuations than the trends of the octupole and decapole components displayed in Fig. 3.10d and Fig. 3.10e.

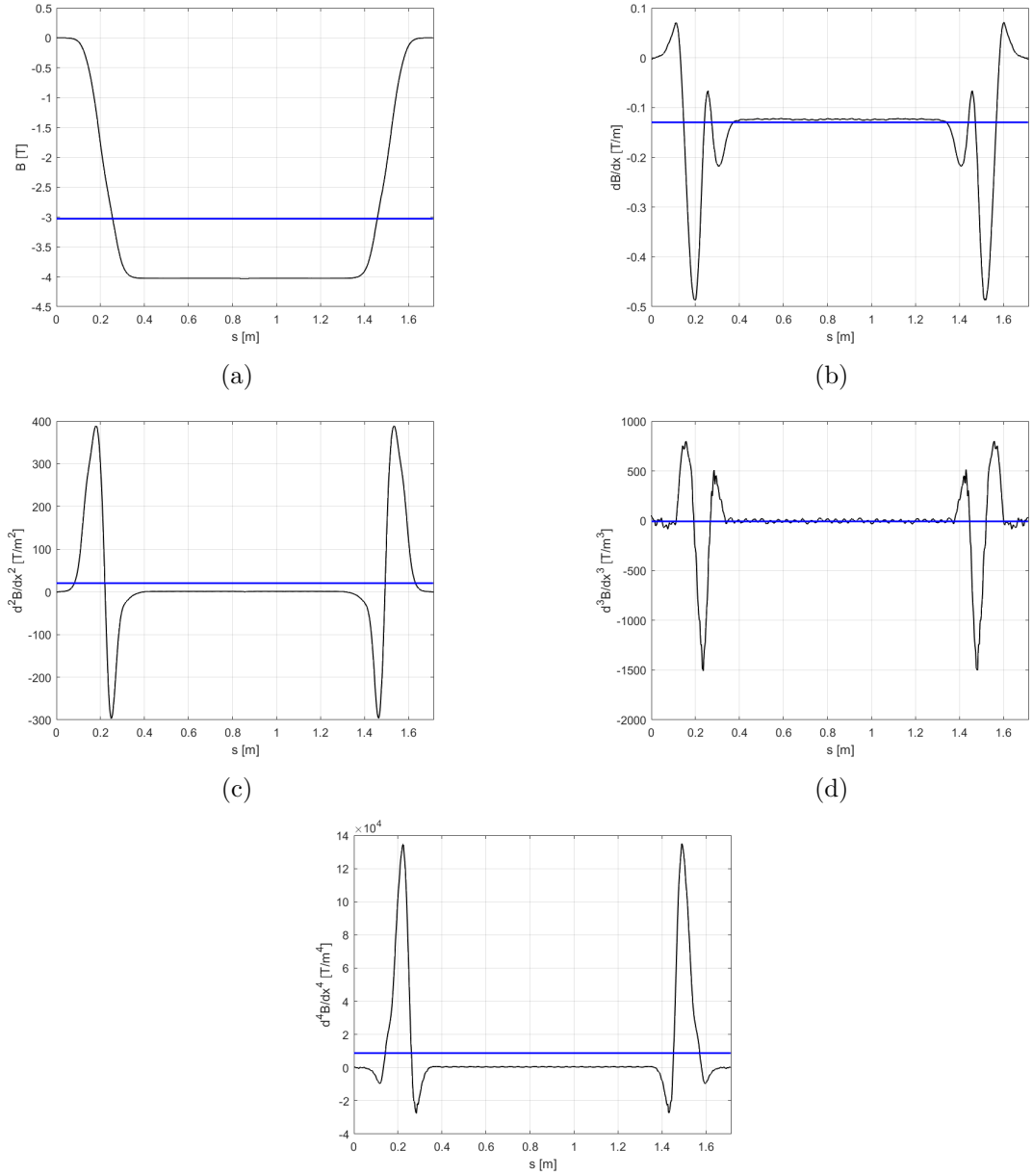

Figure 3.10: (a) The dipole component behaviour plotted along the reference particle trajectory. (b) The quadrupole component behaviour plotted along the reference particle trajectory. (c) The sextupole component behaviour plotted along the reference particle trajectory. (d) The octupole component behaviour plotted along the reference particle trajectory. (e) The decapole component behaviour plotted along the reference particle trajectory. In all figures, the trajectory s of the ideal particle is evaluated with the particle tracking tool and the blue lines represent the values of the average integral calculated by normalizing the integral results for the reference trajectory path.

The multipole coefficients are integrated by introducing the formula Eq. 3.2 and the results are reported in Tab. 3.7. The integral is calculated along s that represents the length of the tracked reference trajectory. The retrieved results are satisfactorily comparable with the ones illustrated in Tab. 3.1.

Integral of Taylor coefficients				
Dipole $[Tm]$	**Quadrupole** $[T/m\ m]$	**Sextupole** $[T/m^2\ m]$	**Octupole** $[T/m^3\ m]$	**Decapole** $[T/m^4\ m]$
-5.19	-0.22	36.26	46.31	2.56×10^5

Table 3.7: Results obtained by the integral of the multipole coefficients considering the tracked reference particle trajectory.

The values of the integrated multipole coefficients are normalized with respect to the length of the reference trajectory evaluated with the particle tracking tool and the results are shown in Tab. 3.8. The average integral outcomes are also graphically illustrated in Fig. 3.10 with the blue lines just to have visual feedback of the data. The results are in agreement with the average integral values reported in Tab. 3.2.

Average integral of Taylor coefficients				
Dipole $[T]$	**Quadrupole** $[T/m]$	**Sextupole** $[T/m^2]$	**Octupole** $[T/m^3]$	**Decapole** $[T/m^4]$
-3.03	-0.13	21.14	27.00	1.50×10^5

Table 3.8: Results obtained by the average integral of the multipole coefficients considering the tracked reference particle trajectory.

The outcomes are converted in field units and the conversion formula Eq. 2.19 is used. The conversion in field units is useful for the comparison with the data retrieved by considering the reference trajectory approximated with an arc of a circle with a radius of curvature $\rho = 1.65$ m and two straight parts simulating the drift regions. The results in field units are displayed in Tab. 3.9 and the value of B_N is the integrated dipole component equal to -5.19 Tm. The weight of the field components in terms of field units is the same reported in Tab. 3.3 where the sextupole field component is the one that has to be reduced to remain in the established range for the field quality. Specifically, the difference between the multipole coefficients expressed in field units calculated considering the trajectory approximated with an arc of a circle and two straight parts and the ones evaluated with the tracked trajectory is much lower than one unit.

Also in the case of the reference trajectory evaluated with the particle tracking tool, the y-component of the magnetic field can be integrated along the toroidal lines introduced in Sec. 3.4. Then, the integrated magnetic field is normalized by considering the length of each toroidal line. The interpolation of the integrated and normalized magnetic field is performed with the MatLab polynomial curve fit. In order to define the multipole

Multipole coefficients in field units				
Dipole [-]	**Quadrupole [-]**	**Sextupole [-]**	**Octupole [-]**	**Decapole [-]**
10000	9.29	-16.29	-0.15	-4.47

Table 3.9: The values of the multipole coefficients converted in field units using the conversion formula Eq. 2.19 and considering the tracked reference particle trajectory.

coefficients of the integrated and normalized field B_y, the results calculated by interpolating the data are multiplied by the factorial of $n-1$, where n is the polynomial degree. The values of the field components are illustrated in Tab. 3.10. Except for the octupole component, the other field components are closely comparable with the data reported in Tab. 3.4.

Taylor coefficients of the integrated and normalized field				
Dipole $[T]$	**Quadrupole** $[T/m]$	**Sextupole** $[T/m^2]$	**Octupole** $[T/m^3]$	**Decapole** $[T/m^4]$
-3.04	-0.13	21.22	27.11	1.50×10^5

Table 3.10: Field components obtained after the interpolation of the data calculated by integrating and normalizing the y-component of the magnetic field considering the tracked reference particle trajectory.

The results shown in Tab. 3.10 are converted in field units using the conversion formula Eq. 2.19. In this case, the main field component B_N is the dipole field component calculated considering the integrated and normalized magnetic field B_y and its value is equal to -3.04 T. The values of the multipole coefficients converted in field units are reported in Tab. 3.11. In terms of field units, the outcomes evaluated by considering the integrated and normalized field B_y are strictly similar to the multipole coefficients results shown in Tab. 3.5, indeed the difference of all field components is much smaller than one field unit.

To demonstrate that both approaches are suitable for the correct analysis of the field quality of a curved magnet, the difference in absolute value of the multipole coefficients converted in field units is calculated and the results are reported in Tab. 3.12. Specifically, the difference is performed by taking into consideration the results reported in Tab. 3.9 and Tab. 3.11. The difference of the dipole component is perfectly equal to zero since the conversion formula introduced for expressing the multipole coefficients in field units is normalized with respect to the main field B_N respectively equal to the integrated dipole field and the integrated and normalized dipole field. The differences of the other high-multipole components are lower than 10^{-3} units which may be regarded as a satisfactory outcome.

As a further conclusion, the values of the average integrals of the coefficients calculated with the Taylor series expansion and the results retrieved by the Taylor expansion

Multipole coefficients in field units				
Dipole [-]	**Quadrupole [-]**	**Sextupole [-]**	**Octupole [-]**	**Decapole [-]**
10000	9.29	-16.29	-0.15	-4.47

Table 3.11: The values of the multipole coefficients converted in field units using the conversion formula Eq. 2.19 and calculated considering the tracked reference particle trajectory. The main field B_N is the value of the integrated and normalized dipole component.

Difference in absolute value				
Dipole [-]	**Quadrupole [-]**	**Sextupole [-]**	**Octupole [-]**	**Decapole [-]**
0	0.0005	0.0007	4.31×10^{-5}	0.0020

Table 3.12: The difference in absolute value of the multipole coefficients retrieved by the two different approaches and expressed in field units. In particular, the difference is performed between the values reported in Tab. 3.9 and Tab. 3.11.

analysis of the integrated and normalized y-component of the magnetic field are in agreement if the reference trajectory of the ideal particle is approximated with an arc of a circle and two straight lines or the reference particle trajectory is computed with the particle tracking tool, i.e. the local tracking is directly performed inside the 3D magnetic field map. Therefore, with good approximation, the field quality of the magnet can be characterized by evaluating the ideal particle trajectory geometrically, taking into account the greater simplicity of the geometric approximation compared to the algorithm employed for particle tracking.

3.6 Reconstruction of the Magnetic Field Map

The magnetic field is commonly described by the main integrated field components and the high-order field coefficients. From a mathematical perspective, the magnetic field representation is an analytical function in a simply-connected domain developed into eigenfunctions with the multipole coefficients [32]. The magnetic field reconstruction inside the domain of interest is useful for analysing the calculation uncertainties and approximations.

The reconstruction of the magnetic field can be performed only on the length of the segment selected for the Taylor expansion analysis set equal to 21.6 mm to be coherent with the particle beam size employed in the tracking to benchmark the field components obtained through the Taylor analysis of the 3D magnetic field map [27] and to be inside the so-called good field region, conventionally defined as two-thirds of the magnet aperture [18].

First, to perform the analysis, the reference trajectory of the ideal particle is approximated by an arc of a circle and two straight parts as thoroughly in Sec. 3.1. Second, the

set of segments perpendicular to the reference trajectory is constructed in order to evaluate the y-component of the magnetic field B_y on each segment. The 3D magnetic field map illustrated in Fig. 3.1a presents an up/down symmetry allowing the reconstruction of the magnetic field considering only the half length of the magnet.

The MatLab function *polyfit* is employed to define the coefficients for a polynomial $p(x)$ of a degree n. Specifically, the x points are the ones identified on the segments and the y data are the ones obtained after manipulating the 3D magnetic field map data from the Opera Simulation Software.

The MatLab function *polyval* is then used to evaluate the polynomial p at each point in x. Specifically, the polynomial p is assessed at the points identified on the set of segments perpendicular to the reference particle trajectory. To properly reconstruct the magnetic field, the MatLab function *scatteredInterpolant* is used to perform the interpolation on a data set of scattered data and it returns an interpolating function F for the given data set. The interpolant F can be evaluated at a set of query points to produce interpolated values. The option "*linear*" is selected for the interpolation method and the extrapolation method is set as "*none*". The representation of the magnetic field values calculated by the interpolating function F at query locations is illustrated in Fig. 3.11 with the red wildcard characters. The values of the polynomial p at each point in x are instead illustrated with blue circles.

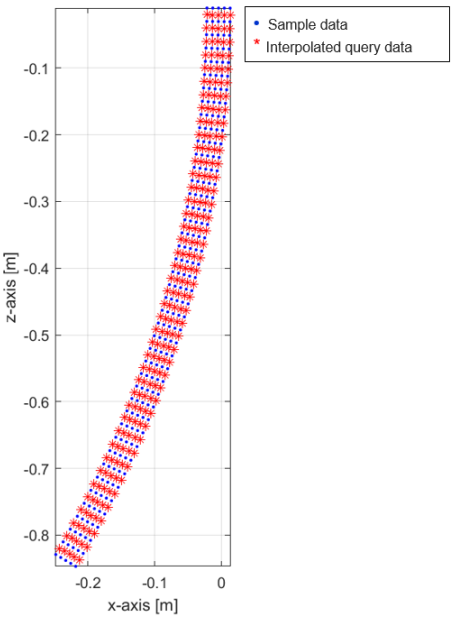

Figure 3.11: Representation of the magnetic field values calculated with the interpolant F at query points (red wildcard characters) and the values of the polynomial p at each point x (blue circles).

To quantify the discrepancy between the magnetic field values calculated with the interpolating function F and the field values obtained from the 3D magnetic field map

evaluated in Opera Simulation Software at the same query locations, the absolute difference in tesla is assessed and the result is illustrated in Fig. 3.12. The critical region is the one in the proximity of the magnet's heads due to their strong contribution that generates non-linear components of the magnetic field that cannot be neglected. The accuracy of the magnetic field reconstruction is in the order of 10^{-4} that is a satisfactory result for the desired precision of the analysis. Concerning the magnetic field quality analysis, this is an additional validation of the Taylor series expansion approximation.

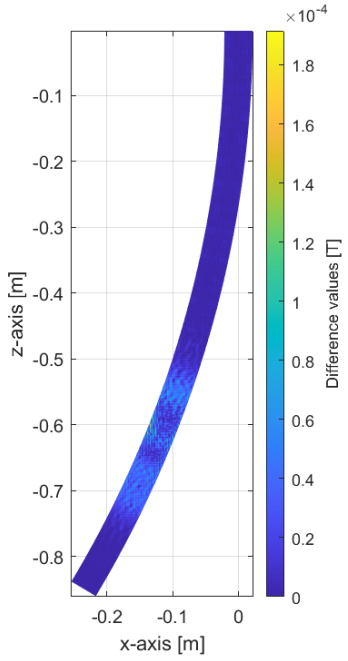

Figure 3.12: Illustration of the absolute difference in tesla between the magnetic field values calculated with the interpolating function F and the values of the 3D magnetic field map at the same query points.

Chapter 4

Fourier Series Expansion

4.1 The Fourier Expansion of the Radial Field Component

Typically for large accelerators, the magnets are straight or can be approximated as such. This is the case of the CERN Large Hadron Collider (LHC), where the dipoles are 15 m long and the heads measure a few percent of the dipole length [33]. The field quality description in such magnets is generally based on cylindrical multipoles, which constitute a full basis for the solution of the Laplace equation in the 2D case [21]. However, the design of short and strongly bent SC dipoles requires an appropriate description of the quality of the produced magnetic field [17]. Although it is common practice to describe the field by introducing cylindrical multipoles in the transverse plane, the curved magnets require further discussion on the validity of this approach. The design of the magnet involved in the analysis is described in Sec. 2.3. As a reminder, the SC combined function dipole analyzed in the present work is based on a main field of 4 T and an aperture ranging from 70 mm up to 90 mm. The beam rigidity of 6.6 Tm yields a bending radius ρ of 1.65 m and the bending angle is equal to 45°, resulting in a magnetic length of about 1.3 m. The 3D magnetic field map evaluated with the Opera Simulation Software is displayed in Fig. 3.1a. The design bending plane is chosen perpendicular to the y-axis. The ideal particle is defined as the particle that follows the nominal geometry of the magnet and that is deflected by the nominal bending angle of 45°. In the following analysis, the trajectory of the ideal particle is approximated by considering an arc of a circle with a radius of curvature ρ of 1.65 m, φ ranging from $-22.5°$ to 22.5° and two straight parts to reach the end of the field map, as described and represented in Sec. 3.1.

With the purpose of determining the field harmonics with the Fourier series expansion approach on the domain boundary, the first step is the definition of the domain of the problem. In the case of accelerator magnets, the domain boundary is often chosen as a circle with a radius of two-thirds of the aperture radius [19]. In this work, the selected reference radius r_0 is equal to 21.6 mm in order to remain inside a region in which, as a first approximation, the magnetic field behaves properly and to guarantee the comparability of the field harmonics with the multipole coefficients approximated with a suitable Taylor series expansion of the flux density at the horizontal median plane. To evaluate the multipole coefficients or the field harmonics A_n and B_n, the radial component of the

magnetic flux density can be used. Firstly, a set of circles orthogonal to the reference particle trajectory, approximated with an arc of a circle and two straight parts, is defined. To properly evaluate the radial field component B_r, the magnetic field component orthogonal to the ideal particle trajectory is calculated on each circle and it is called the rotated field component $B_{x,rot}$. Specifically, the rotated component $B_{x,rot}$ can be expressed in terms of the x-component and the z-component of the magnetic flux density as shown in Eq. 4.1 where α is the angle that identifies the longitudinal position along the particle trajectory (see Fig. 4.1).

$$B_{rot} = B_x \; cos\alpha + B_z \; sin\alpha \tag{4.1}$$

The value of the radial field component B_r of the magnetic flux density at a reference radius $r = r_0$ equal to 21.6 mm as a function of the angular position φ is obtained, on each circle, by associating the $B_{x,rot}$ component and the y-component B_y.

$$B_r(r_0, \varphi) = B_y \; sin\varphi + B_{rot} \; cos\varphi \tag{4.2}$$

Then, the radial field component can be expressed with the Fourier series expansion. The set of circles on which the radial field component B_r is assessed is built perpendicularly with respect to the reference trajectory and it is illustrated in Fig. 4.1 where the colour bar indicates the values of the radial field component in tesla. As expected, the radial field component decreases down to 0 T.

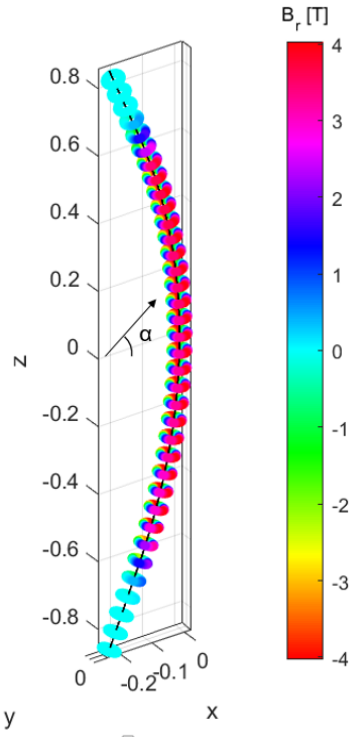

Figure 4.1: Illustration of the set of circles transverse to the reference particle trajectory s approximated with an arc of a circle and two straight parts. The colour bar on the right indicates the values of the radial field component B_r in tesla.

The Fig. 4.2 shows the values of the radial field component, expressed in tesla, on a circle selected in the central region of the magnetic field map. The radius of the circle is the reference one r_0 = 21.6 mm. The behaviour of B_r, as a function of the angular position φ, ranges from -4 T to 4 T.

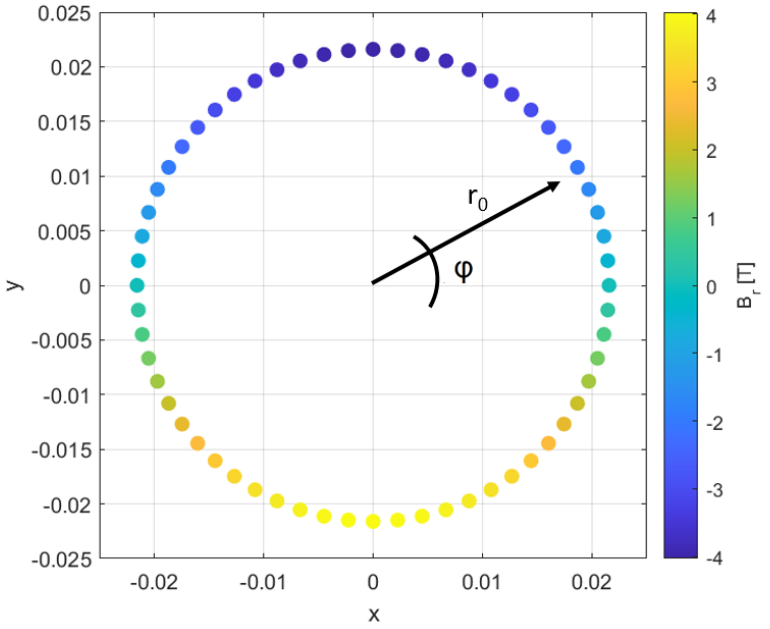

Figure 4.2: Illustration of the values of the radial field component B_r expressed in tesla on a circle located in the central region of magnetic field map.

The normal and skew multipole coefficients $B_n(r_0)$ and $A_n(r_0)$ at a reference radius r_0 equal to 21.6 mm are evaluated by using the relations introduced in Eq. 2.13 and Eq. 2.14. In computational practice, the component B_r is numerically calculated at N discrete points in the interval [0,2π) and the multipole coefficients $A_n(r_0)$ and $B_n(r_0)$ are assessed by introducing the *discrete Fourier transform* [19]:

$$A_n(r_0) \approx \frac{2}{N} \sum_{k=0}^{N-1} B_r(r_0, \varphi_k)\ cos\ n\varphi_k \tag{4.3}$$

$$B_n(r_0) \approx \frac{2}{N} \sum_{k=0}^{N-1} B_r(r_0, \varphi_k)\ sin\ n\varphi_k \tag{4.4}$$

where $\varphi_k = \frac{2\pi k}{N}$ with k = 0,1,2, ..., $N-1$. To guarantee sufficient accuracy for the calculation of the skew and normal coefficients up to order n =15, the number of discrete points N is set equal to 60 [19]. In the present work, the multipole coefficients are taken into account up to the order n =5 considering that the coefficients after the decapole component are negligible as discussed in Appendix A. Assuming field symmetry about

the median plane, the skew multipole components $A_n(r_0)$ are expected to be null. The distributions of the normal multipole components $B_n(r_0)$ are represented in Fig. 4.3. The coefficient $n = 1$ represents the dipole field. The other field components are illustrated by normalizing the multipole under consideration for the reference radius r_0 raised to $n - 1$.

The behaviour of the dipole component is coherent with the trend illustrated in Fig. 3.5a where the field component is evaluated by the comparison with the Taylor coefficients of a series expansion of the magnetic flux density. As expected, the value of the dipole field component is equal to 4 T inside the body of the magnet. The higher-order multipole coefficients exhibit relevant differences with respect to the field harmonics represented in Fig. 3.5. In particular, the quadrupole field component displays two negative peaks and, as a consequence, the quadrupole gradient is higher than the one evaluated with the Taylor expansion equal to -0.12 T/m. The sextupole and the decapole components differ slightly in the trend with respect to the Fig. 3.5c and Fig. 3.5e, however, the numerical results are not comparable with the outcomes of the average integrals of the Taylor expansion coefficients reported in Tab. 3.2. Concerning the octupole component, both the plot and the numerical outcome are not analogous with the results retrieved in Sec. 3.2 and Sec. 3.3.

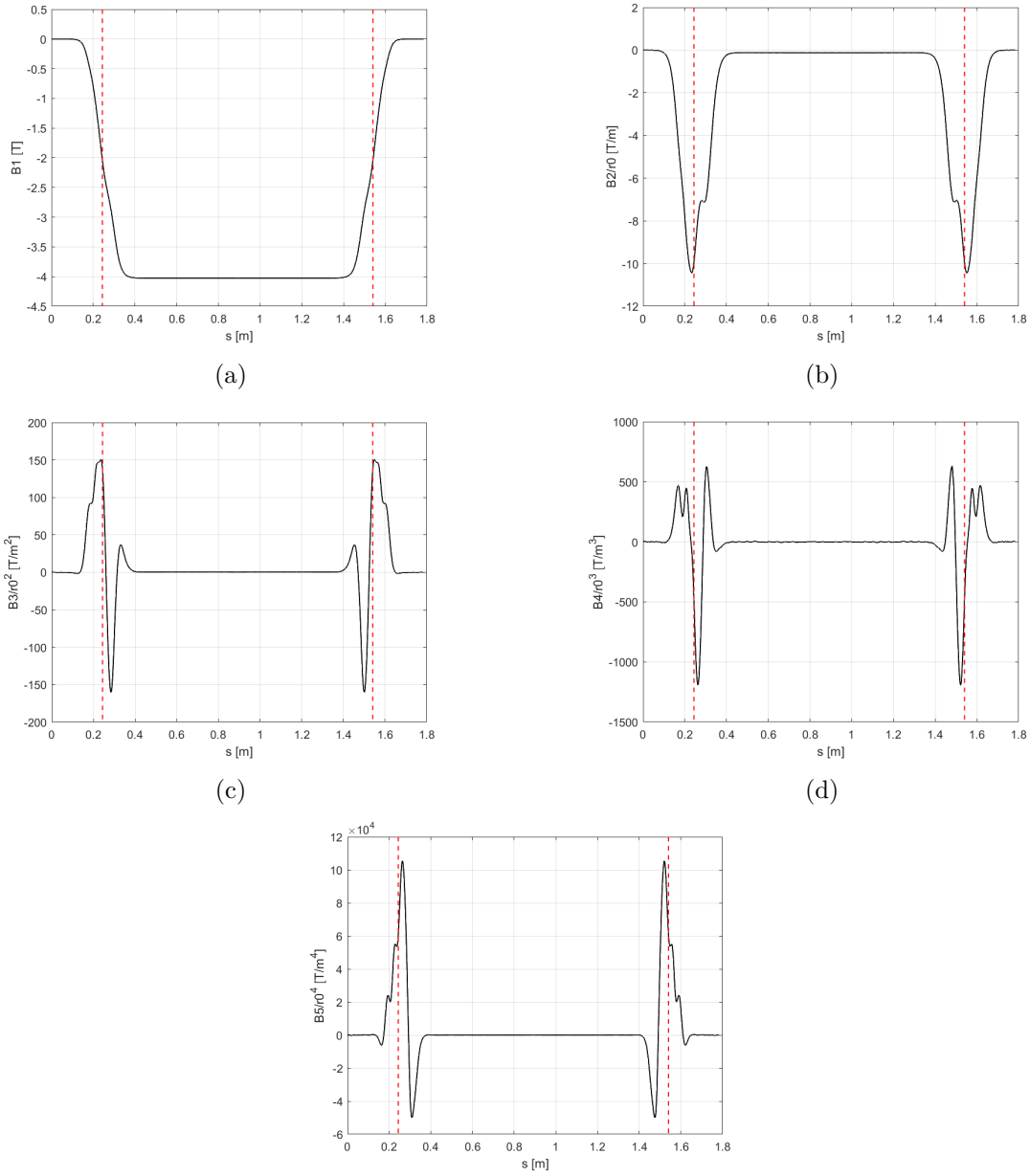

Figure 4.3: (a) Representation of the dipole component behaviour B_1 in T plotted along the reference trajectory. (b) Representation of the quadrupole component behaviour B_2 in T/m plotted along the reference trajectory. (c) Representation of the sextupole component behaviour B_3 in T/m^2 plotted along the reference trajectory. (d) Representation of the octupole component behaviour B_4 in T/m^3 plotted along the reference trajectory. (e) Representation of the decapole component behaviour B_5 in T/m^4 plotted along the reference trajectory. In all figures, the red dashed lines indicate the points at $\pm 22.5°$ that represent the range of the angle φ.

To compare numerically the field harmonics determined with the Fourier series expansion of the radial field component with the multipole coefficients evaluated by comparison with the Taylor coefficients of a series expansion of the magnetic field at the median plane, the mean value of the normal multipole components is evaluated as $\frac{1}{N}\sum_{i=1}^{N} B_{ni}$, where N is the total number of observation points. The results are reported in Tab. 4.1 considering that each normal multipole component is divided by the reference radius r_0 raised to $n-1$.

Mean value of the B_n coefficients				
Dipole $[T]$	**Quadrupole** $[T/m]$	**Sextupole** $[T/m^2]$	**Octupole** $[T/m^3]$	**Decapole** $[T/m^4]$
-2.91	-1.65	16.59	22.20	1.08×10^5

Table 4.1: Results retrieved by calculating the mean value of the normal multipole coefficients B_n divided by the reference radius r_0 raised to $n-1$.

The results calculated by evaluating the mean value of the normal multipole components B_n and then normalizing for the reference radius to the power of $n-1$ differ completely from the average integral values reported in Tab. 3.2 except for the dipole field component that yields the same result.

To guarantee the correct evaluation of the radial field component and consequently of the multipole coefficients, the component B_{rec} is calculated by employing the Eq. 2.11 also reported here:

$$B_{rec}(r_0,\varphi) = \sum_{n=1}^{\infty}(B_n(r_0)\sin n\varphi + A_n(r_0)\cos n\varphi)$$

where the skew and multipole components $A_n(r_0)$ and $B_n(r_0)$ are determined with the Eq. 4.4 and Eq. 4.3. The difference expressed in tesla between the radial field component B_r evaluated with the rotated component $B_{x,rot}$ and the y-component B_y and the reconstructed radial field component B_{rec} calculated with the harmonic components $A_n(r_0)$ and $B_n(r_0)$ is graphically represented in Fig. 4.4. The accuracy achieved with the evaluated difference is on the order of 10^{-4} and the result is acceptable for the purpose of the analysis.

Although the radial field component is supposed to be correctly evaluated, the description and the characterization of the magnetic field in the curved magnet based on the cylindrical multipoles lead to a questionable interpretation of the results. In the case of curved magnets, using field derivatives rather than cylindrical multipoles is suitable to characterize the field and analyse the field quality requirements. Moreover, the field derivatives are directly used by beam optics calculations thus promoting and facilitating the dialogue between magnet and accelerator designers [21].

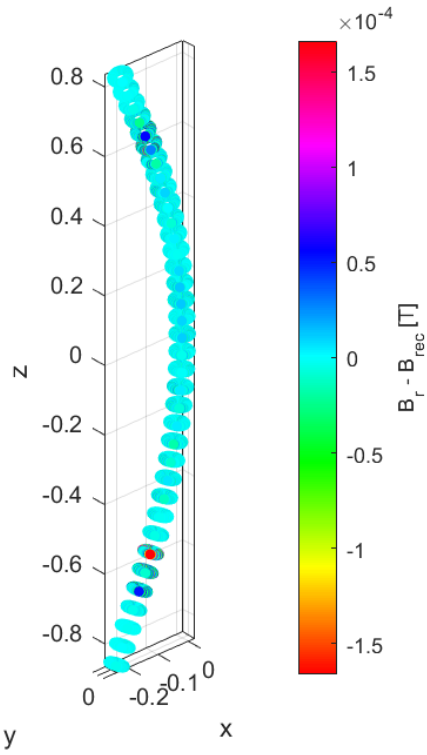

Figure 4.4: Illustration of the difference between the radial field component B_r and the reconstructed radial component B_{rec} expressed in tesla.

4.2 The Scaling Law of the Multipole Coefficients

The scaling law of multipole coefficients to any radius r inside the magnet aperture was verified to exclude an evaluation error for the field harmonics' distributions related to the choice of the reference radius r_0 initially imposed equal to 21.6 mm for the determination of the multipoles with the Fourier series expansion approach.

First, a preliminary analysis is carried out to validate the scaling laws in the case of a strongly bent magnet performing the evaluation of the multipole coefficients at radii lower than the reference one r_0; second, the scaling laws are used to verify the extension of the good field region (GFR) calculating the normal and the skew components at radii higher than the reference one.

The scaling laws are based on multipole coefficients evaluated earlier at the same reference radius $r_0 = 21.6$ mm and they are expressed as:

$$\overline{A_n}(r_k) = \left(\frac{r_k}{r_0}\right)^{n-1} A_n(r_0) \tag{4.5}$$

$$\overline{B_n}(r_k) = \left(\frac{r_k}{r_0}\right)^{n-1} B_n(r_0) \tag{4.6}$$

where $\overline{A_n}(r_k)$ and $\overline{B_n}(r_k)$ are the skew and normal multipole coefficients calculated at any radius r_k inside the aperture. The field scaling is tested at 4 radii 2 mm apart in the range of 15.6 to 21.6 mm. The coefficient n corresponds to the field harmonic distributions and $A_n(r_0)$ and $B_n(r_0)$ are the skew and normal multipole components evaluated with the integral of the radial field component B_r as introduced in Eq. 2.13 and Eq. 2.14 and also reported below:

$$A_n(r_0) = \frac{1}{\pi}\int_0^{2\pi} B_r(r_0,\varphi)\cos n\varphi\, d\varphi \qquad n = 1,2,3...$$

$$B_n(r_0) = \frac{1}{\pi}\int_0^{2\pi} B_r(r_0,\varphi)\sin n\varphi\, d\varphi \qquad n = 1,2,3...$$

where, for instance, $n = 1$ corresponds to the dipole field component.

To validate the scaling laws, the skew and normal multipole coefficients $A_n(r_k)$ and $B_n(r_k)$ are therefore calculated at each radius r_k inside the magnet aperture with the integral of the radial field component $B_r(r_k,\varphi)$ as:

$$A_n(r_k) = \frac{1}{\pi}\int_0^{2\pi} B_r(r_k,\varphi)\cos n\varphi\, d\varphi \qquad n = 1,2,3... \tag{4.7}$$

$$B_n(r_k) = \frac{1}{\pi}\int_0^{2\pi} B_r(r_k,\varphi)\sin n\varphi\, d\varphi \qquad n = 1,2,3... \tag{4.8}$$

where, once again, the radius r_k goes from 21.6 mm up to 15.6 mm with a step of 2 mm, thus moving inwards through the aperture.

The distributions of the normal multipole coefficients evaluated with the scaling law and with the integral of the radial field component at each radius r_k are graphically represented in Fig. 4.5 to qualitatively observe the presence of some divergences. Concerning

the dipole field component, it remains constant since in the scaling law of multipole coefficients n is equal to one and consequently the ratio $(r/r_0)^{n-1}$ is always equal to 1. The quadrupole and the sextupole field components (see Fig. 4.5) are shown to analyse the scaling law's consistency. The quadrupole distributions, evaluated with the scaling law $\overline{B_n}(r_k)$ and with the integral of the radial field component $B_n(r_k)$, are illustrated in Fig. 4.5a. In the body of the magnet, the difference between the two evaluation approaches is roughly null whereas, in the magnet's heads, where the determination of the field harmonics becomes more complicated with the Fourier expansion method, the curve differences need to be carefully monitored. Concerning the distributions of the sextupole component evaluated at different radii starting from the reference one 21.6 mm up to 15.6 mm using a step equal to 2 mm, the difference between the field components evaluated with the scaling law $\overline{B_n}(r_k)$ and the ones directly calculated with $B_n(r_k)$ presents irrelevant discrepancies in the body of the magnet while, in the region of the heads, some variation can be observed. The illustration of the sextupole field distributions considering the two different evaluation approaches is reported in Fig. 4.5b. All the field distributions are represented considering $B_n(r_k)/(r_k)^{n-1}$, i.e. normalizing the normal coefficients for the radius under analysis raised to $n-1$ where n corresponds to a specific field distribution.

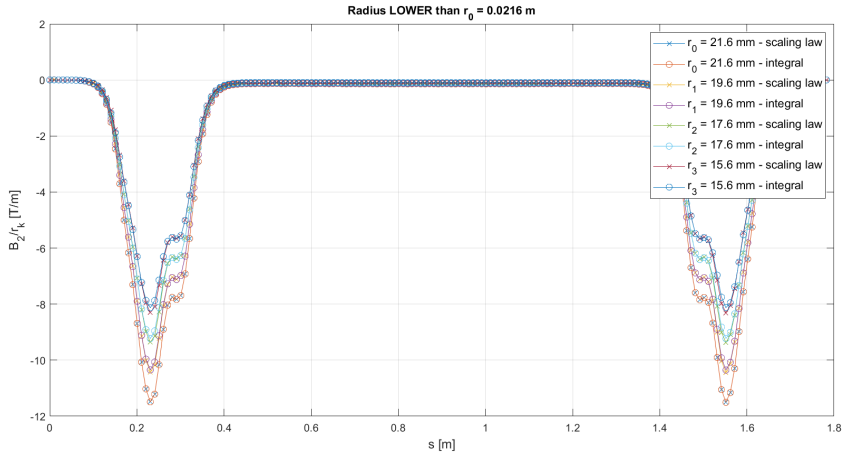

(a)

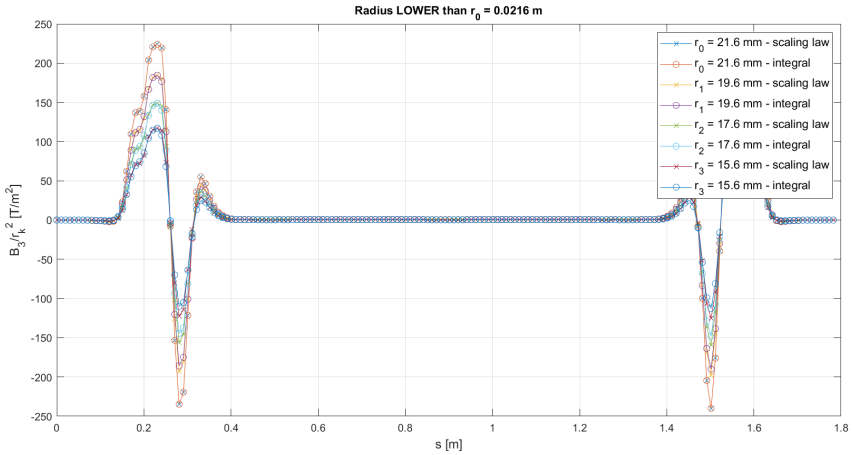

(b)

Figure 4.5: (a) Representation of the quadrupole field distributions evaluated with the scaling law of the multipole coefficients and with the integral of the radial field component calculated at each analysis radii. (b) Representation of the sextupole field distributions evaluated with the scaling law of the multipole coefficients and with the integral of the radial field component calculated at each analysis radii. All the curves are plotted with respect to the reference trajectory s of the ideal particle.

To numerically quantify the discrepancies between the field distributions evaluated with the scaling law of the multipole coefficients expressed with Eq. 4.5 and Eq. 4.6 and the ones determined with the integral of the radial field component $B_r(r_k)$, the absolute difference in field units is calculated between the results retrieved by the two approaches. To consistently compare the normal multipole coefficients computed with the scaling law and directly with the integral, the mean value of the dipole field determined with the Fourier expansion of the radial component B_r at a reference radius $r_0 = 21.6$ mm is used as the main field component B_N and it is equal to -2.91 T. Such a choice is also related to the distributions of the dipole component B_1 and the other high-order coefficients that assume values around zero in the region of the magnet heads and consequently, B_1 should not be selected as the main field component B_N (see Eq. 2.19 as reference) in order to avoid numerical errors.

The differences, determined for the quadrupole and the sextupole field components and expressed in field units, have relatively high values in the region of the magnet's heads, especially for analysis radii equal to 17.6 mm and 15.6 mm. The reason could be related to the uncertainty introduced a priori in the evaluation of these components at the coil's heads. In the body of the magnet, the evaluated differences are lower than one unit as a confirmation of the satisfactory comparison achieved between the multipole coefficients calculated with the Fourier series expansion of the radial field component and the field harmonics computed with a suitable Taylor series expansion. These field components' differences are illustrated in Fig. 4.6a and Fig. 4.6b. Concerning the octupole field component illustrated in Fig. 4.6c, the differences evaluated in the magnet's heads are approximately equal to one field unit whereas in the body of the magnet are lower than the unit. The reason could be related to the unit value of the octupole component of -0.12, significantly lower than one field unit. In conclusion, the scaling law of the multipole coefficients is verified taking into account the evaluation uncertainty of the field harmonics in the coil's head region.

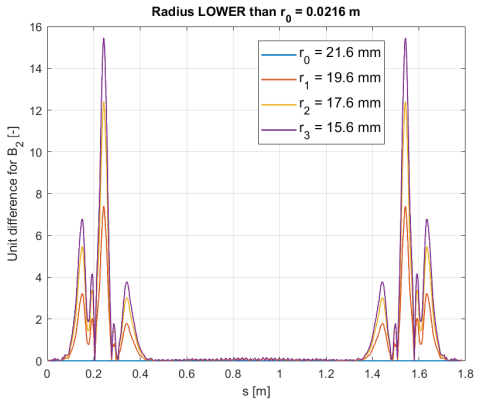

(a)

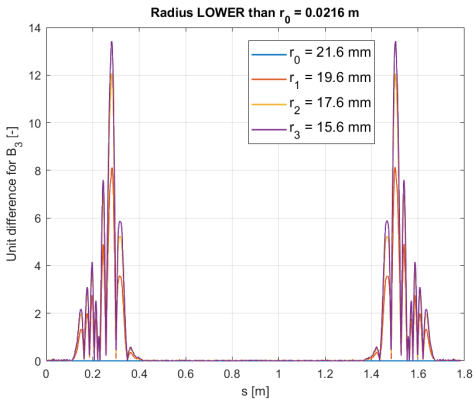

(b)

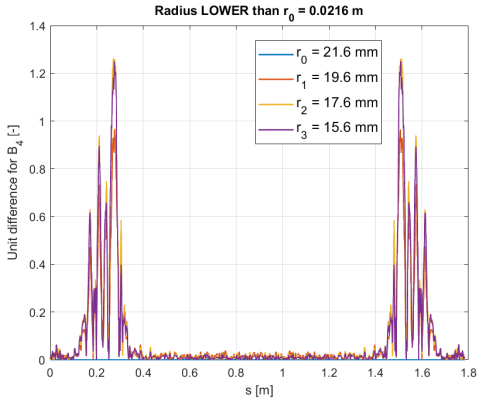

(c)

Figure 4.6: (a) Differences evaluated for the quadrupole distributions. (b) Differences evaluated for the sextupole distributions. (c) Differences evaluated for the octupole distributions. All the curves are plotted with respect to the reference trajectory s of the ideal particle and the differences are converted into field units for all the field harmonics. The analysis radii r_k are selected lower than the radius of 21.6 mm to certainly remain inside the good field region, specifically r_k = 19.6 mm, 17.6 mm, 15.6 mm.

The scaling law of the multipole coefficients can be applied to the extension verification of the good field region (GFR). To qualitatively identify the good field region of the magnet, two-thirds of the aperture radius is calculated. This value is conventionally used by the magnet design community to evaluate the good field region. In the dipole currently analysed, the radius of the aperture is equal to 40 mm and thus the size for the good field region can be identified as 26.7 mm. The blue line in Fig. 4.7 represents y-component of the magnetic field versus the x-axis and it can be noticed the presence of strongly high-order field components in close proximity to the good field region limits.

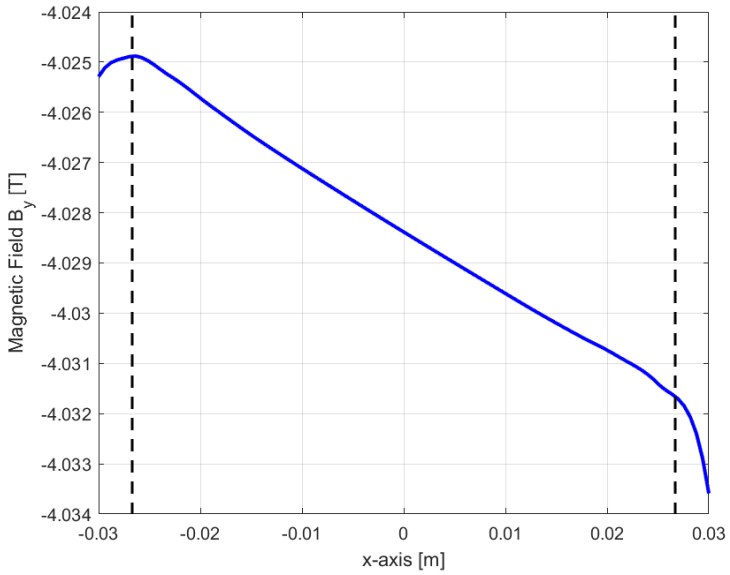

Figure 4.7: Illustration of the y-component of the magnetic field in tesla versus the x-axis in the centre of the magnet (blue line). The dashed vertical lines in black indicate the points at $\pm$ 26.7 mm, i.e. the two-thirds of the aperture radius.

As a verification, the field harmonics calculated with scaling laws reported in Eq. 4.5 and Eq. 4.6 are compared with the multipole coefficients determined with the integral of the radial field component $B_r(r_k)$ calculated at each analysis radii r_k higher than the reference one equal to 21.6 mm and in particular r_k = 25.6 mm, 29.6 mm, 33.6 mm. The differences of the field harmonics, expressed in field units, are calculated by considering only the body of the magnet, where the multipoles evaluated with a Fourier series expansion of the radial component B_r are punctually comparable with the ones determined by employing a Taylor series expansion of the calculated field at a symmetry axis. The differences representation is graphically illustrated in Fig. 4.8 and the evaluation is performed by roughly varying φ from $-16°$ up to $16°$, i.e. a region far enough away from the heads of the magnet.

In all the multipole coefficients represented, the differences between the curves evaluated with the scaling law and the ones determined with the integral of the radial field component $B_r(r_k)$ are lower than one field unit when the radius is equal to 25.6 mm.

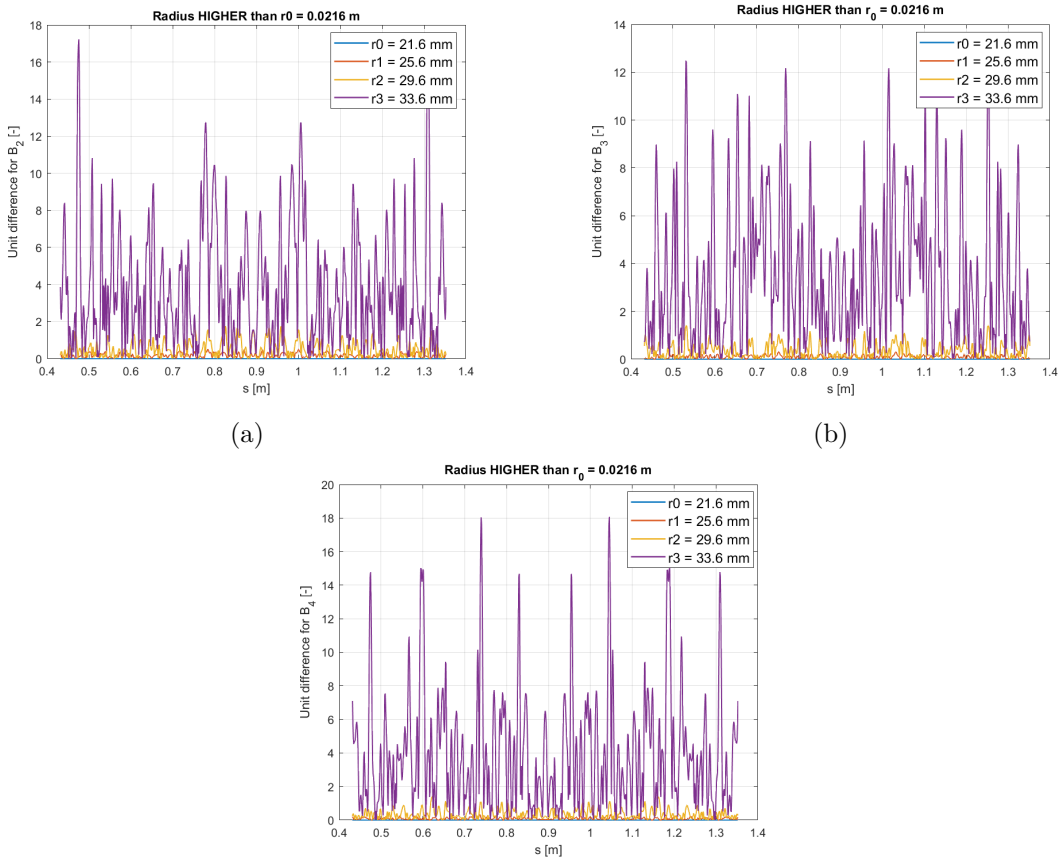

Figure 4.8: (a) Differences evaluated for the quadrupole distributions. (b) Differences evaluated for the sextupole distributions. (c) Differences evaluated for the octupole distributions. All the curves are plotted with respect to the reference trajectory s of the ideal particle considering only the body of the magnet where φ ranges approximately from $-16°$ to $16°$. The values of the difference are converted into field units for all the field harmonics. The analysis radii are selected higher than the radius of 21.6 mm to reach the boundary of the good field region, specifically r_k = 25.6 mm, 29.6 mm, 33.6 mm.

Considering a radius higher than the latter, the difference expressed in field units increases; for instance, the difference of the quadrupole component at a radius of 33.6 mm is higher than 10 field units.

An accurate analysis is performed between a reference radius r_0 at 25.6 mm and 33.6 mm with a 1 mm step in order to have clear evidence of the extension of the good field region. The results of this analysis are illustrated in Fig. 4.9. The procedure involves evaluating the average of the absolute unit difference between the multipole coefficients determined with the integral of the radial field component $B_r(r_k)$ and the ones calculated with the scaling law $\overline{B_n}(r_k)$. The evaluation is carried out by varying the variable φ from

$-16°$ to $-16°$, i.e. a region that identifies the body of the dipole thus quite far from the coils' heads. In the graph, the red line represents one field unit value. The outcomes of the average unit difference of the multipole coefficients are represented at different reference radii. The analysis results underline that the agreement between the evaluation of the field harmonics with the scaling law $\overline{B_n}(r_k)$ and with the integral of $B_r(r_k)$ is verified up to a radius of 29.6 mm where the average unit difference of high-order multipole coefficients is lower than one unit. Instead, considering a radius of 30.6 mm, the average unit difference for the dipole and the quadrupole components tends to be higher than one unit field.

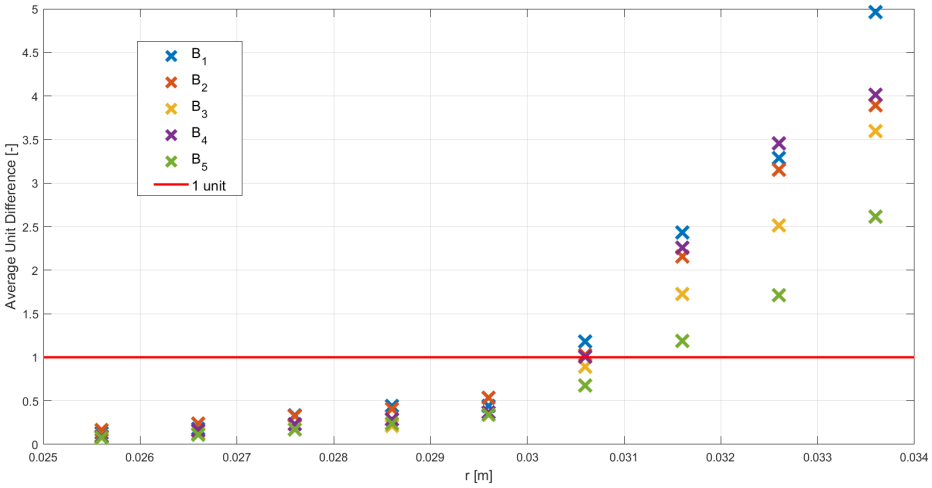

Figure 4.9: Representation of the average unit difference results for the multipole coefficients from the dipole up to the decapole component plotted with respect to different analysis radii, specifically r_k = 25.6 mm, 26.6 mm, 27.6 mm, 28.6 mm, 29.6 mm, 30.6 mm, 31.6 mm, 32.6 mm, 33.6 mm.

4.3 The Integrated Multipole Coefficients

If only the two lowest order elements are used for steering the beam, forces on the particles are either constant or vary linear with the distance from the origin. This is called linear beam optics. It has to be noted that the treatment of each harmonic separately is a mathematical abstraction. In practical situations, many harmonics will be present and many of the coefficients will be non-vanishing. A successful magnet design will, however, minimize the unwanted terms to small values. Therefore, tolerance thresholds for the high-order field harmonics need to be defined. However, in the magnet extremities, there is a non-negligible magnetic field in the axial direction and the multipole coefficients do not satisfy the 2D Laplace's equation. Once again, the normal and skew multipole coefficients $B_n(r_0, z)$ and $A_n(r_0, z)$, evaluated at some longitudinal position z, can be derived by considering the Fourier series expansion of the radial field component $B_r(r_0, \varphi, z)$. However, the scaling laws of the multipole coefficients, discussed in the previous Sec. 4.2 and reported in Eq. 4.5 and Eq. 4.6, cannot be applied to the 3D field harmonics. Anyway, the problem can be overcome by calculating the integrated transverse multipole coefficients [19].

It is relevant to highlight that both magnetic scalar and vector potentials can be used for the formulation of a boundary value problem in the aperture of an accelerator magnet free of currents and magnetized material. In two dimensions, both formulations provide a scalar Laplace equation for the magnetic scalar potential ϕ_m and for the magnetic vector potential A_z [19].

To return to the previous discussion, as described above, the scalar potential in the magnet aperture satisfies the Laplace equation [19]:

$$\Delta^2 \phi_m(x, y, z) = \frac{\partial^2 \phi_m(x, y, z)}{\partial x^2} + \frac{\partial^2 \phi_m(x, y, z)}{\partial y^2} + \frac{\partial^2 \phi_m(x, y, z)}{\partial z^2} = 0 \tag{4.9}$$

The parameter $\overline{\phi}_m(x, y)$ can be defined as:

$$\overline{\phi}_m(x, y) = \int_{-z_0}^{z_0} \phi_m(x, y, z) dz \tag{4.10}$$

Therefore, the Eq. 4.9 can be written as:

$$\Delta^2 \overline{\phi}_m(x, y) = \frac{\partial^2 \overline{\phi}_m(x, y)}{\partial x^2} + \frac{\partial^2 \overline{\phi}_m(x, y)}{\partial y^2} = 0 \tag{4.11}$$

The Eq. 4.11 can be considered valid if the magnet is symmetric with respect to the centre or the integration path is extended far enough outside the magnet so that the field is null. At this point, the scaling laws of the multipole coefficients (Eq. 4.5 and Eq. 4.6) can be applied to the integrated multipoles derived from $\overline{\phi}_m$. Moreover, the Eq. 4.11 can

be written as:

$$\Delta^2\overline{\phi}_m(x,y) = \frac{\partial^2\overline{\phi}_m(x,y)}{\partial x^2} + \frac{\partial^2\overline{\phi}_m(x,y)}{\partial y^2} = \int_{-z_0}^{z_0}\left(\frac{\partial^2\phi_m}{\partial x^2} + \frac{\partial^2\phi_m}{\partial y^2}\right)dz$$
$$= \int_{-z_0}^{z_0}\left(-\frac{\partial^2\phi_m}{\partial z^2}\right)dz = -\frac{\partial\phi_m}{\partial z}\Bigg|_{-z_0}^{z_0}$$
$$= H_z(-z_0) - H_z(z_0) = 0 \tag{4.12}$$

The Eq. 4.12 is fulfilled for symmetric magnets where $H_z(z_0) = -H_z(-z_0)$, i.e. symmetric with respect to the axis origin, or for longitudinal field component that has dropped to zero [19].

Concerning the short and strongly curved dipole with a high contribution of non-linear field components due to the non-negligible influence of the coil's heads involved in the analysis of the field quality, the mathematical treatment previously discussed is not considered valid despite the extension of the integration path, i.e. the toroidal lines, ensures that the field components at the end of the magnetic field map are roughly null and the longitudinal component of the magnetic field satisfy the symmetry resulting from Eq. 4.12. The 3D representation of the toroidal lines is illustrated in Fig. 4.10.

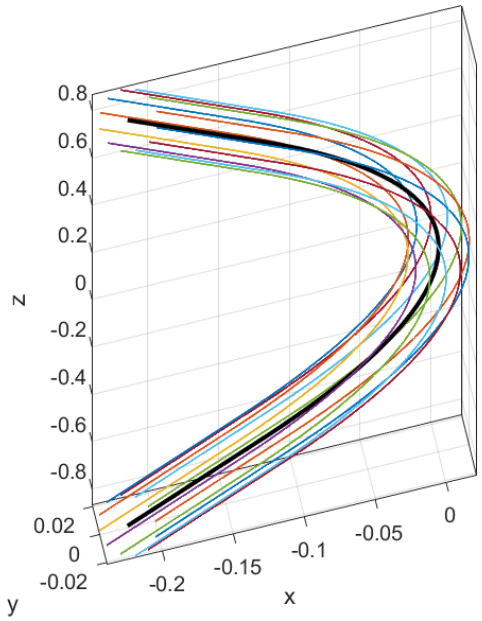

Figure 4.10: Representation of the so-called toroidal lines in a 3D plot. The thicker black line in the plot is the reference trajectory s of the ideal particle, i.e. the particle that follows the geometric orbit of the magnet.

Before proceeding with the evaluation of the multipole coefficients A_n and B_n, the radial component of the magnetic field B_r, assessed at a reference radius $r_0 = 21.6$ mm on

each circle transverse to the reference particle trajectory and calculated by introducing the rotated component $B_{x,rot}$ and the y-component B_y, is integrated and then normalized on each toroidal line (see Eq. 4.13) in order to obtain an equivalent circle cross-section on which the Fourier series expansion analysis can be performed. Specifically, the normalization of the integrated radial field component is assessed by considering the number of points into which each toroidal line is divided to take into account the different path lengths of the toroidal lines. The integrated and normalized field component $B_{r,int}$ for the i-th toroidal line is reported in Eq. 4.13:

$$B_{r,int}(r_0,\varphi_i) = \frac{1}{s_{tot,i}} \int_0^{s_{tot,i}} B_r(r_0,\varphi_i)\, ds_i \approx \frac{1}{N_{tot}} \sum_{j=1}^{N_{tot}} B_r(r_0,\varphi_i)\Delta s_i \tag{4.13}$$

where $s_{tot,i}$ is the total length of the i-th toroidal line, N_{tot} is the total number of j-th points identified on the toroidal lines. Each toroidal line is defined with equally steps Δs_i.

Therefore, the skew and normal multipole coefficients A_n and B_n are evaluated at a reference radius r_0 by considering the integration of the integrated and normalized radial field component $B_{r,int}$ with φ ranging from 0 to 2π as:

$$A_n(r_0) = \frac{1}{\pi} \int_0^{2\pi} B_{r,int}(r_0,\varphi) \cos n\varphi \, d\varphi \qquad n = 1,2,3... \tag{4.14}$$

$$B_n(r_0) = \frac{1}{\pi} \int_0^{2\pi} B_{r,int}(r_0,\varphi) \sin n\varphi \, d\varphi \qquad n = 1,2,3... \tag{4.15}$$

where $n = 1$ corresponds to the dipole field component. In computational practice, the integrated and normalized radial field components are numerically calculated at N discrete points in the interval $[0,2\pi)$ as discussed in Sec. 4.1 and then the evaluation of the multipole coefficients $A_n(r_0)$ and $B_n(r_0)$ is computed by using the discrete Fourier transform.

Just as an example, the results of the quadrupole and sextupole components calculated at a reference radius r_0 equal to 21.6 mm are graphically represented in Fig. 4.11. All the comments are also applicable to the other high-order components not explicitly shown. The graphs report the values of the quadrupole and sextupole field components evaluated with the integral of the integrated and normalized radial field component $B_{r,int}$ and the outcomes of the same multipole coefficients retrieved by the Fourier series expansion of the radial field component B_r.

Specifically, to compare the quadrupole and the sextupole components calculated by using the $B_{r,int}(r_0,\varphi)$ and the same ones evaluated with the Fourier series expansion of $B_r(r_0,\varphi)$, the mean values of the latter multipoles are performed as $\frac{1}{N}\sum_{i=1}^{N} B_{ni}$, where N is the total number of observation points. The field harmonics are then represented by dividing the retrieved values for the reference radius r_0 raised to $n-1$ according to the multipole considered; for instance, the quadrupole component requires that the radius is raised to 1 and therefore, its unit of measure is T/m. Concerning the multipole coefficients evaluated with $B_{r,int}(r_0,\varphi)$, the outcomes retrieved are practically similar to the ones evaluated with the Fourier series expansion of the radial field component $B_r(r_0,\varphi)$.

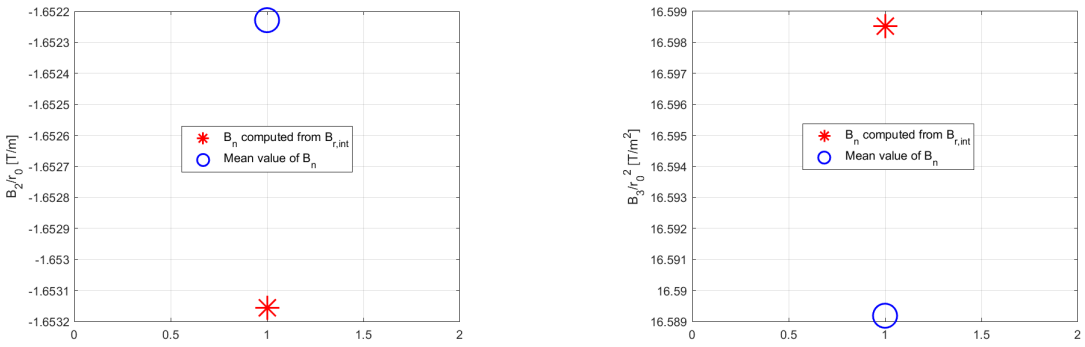

(a) (b)

Figure 4.11: (a) Comparison between the mean value of B_2 and the same quadrupole component calculated with $B_{r,int}$. (b) Comparison between the mean value of B_3 and the same sextupole component calculated with $B_{r,int}$.

4.4 Comparison with Taylor Expansion Results

The great agreement between the average integral of the Taylor expansion coefficients and the Taylor coefficients of the integrated and normalized magnetic field B_y demonstrates that the two approaches are consistent with each other. To simplify the comparison of the retrieved field harmonics with the coefficients evaluated with the Fourier expansion analysis, only the outcomes calculated with one of the two Taylor expansion approaches are considered. The same comment on the retrieved results can be done for the field harmonics evaluated with the Fourier expansion of the radial field component $B_r(r_0, \varphi)$ and the multipole coefficients calculated with the integrated and normalized field component $B_{r,int}(r_0, \varphi)$, therefore only the coefficients results of one of the two Fourier expansion approaches is taken into account for the above-mentioned comparison.

The comparison between the approximated field harmonics from the coefficients in a suitable Taylor series expansion and the multipole coefficients evaluated by using a Fourier series expansion of a field component along a circle is performed by adapting the conversion formula Eq. 2.19 as:

$$\Delta units = b_n - \frac{r^{n-1}}{B_N} \frac{1}{(n-1)!} \frac{d^{n-1} B_y}{dx^{n-1}} \bigg|_{x=y=0} \tag{4.16}$$

where $\Delta units$ indicates the difference in field units between the multipole coefficients and those in the Maclaurin series [19].

The evaluation of the difference, graphically illustrated in Fig. 4.12, highlights that, in the body of the magnet, the assessment accuracy of the multipole coefficients with the two different approaches is below one unit, a quite satisfactory result. However, the same achievement is not reached in the heads of the magnet where the difference between the multipole coefficients respectively determined with the Fourier and Taylor expansion approaches is strongly visible. In addition, the comparison illustrated in Fig. 4.13 between

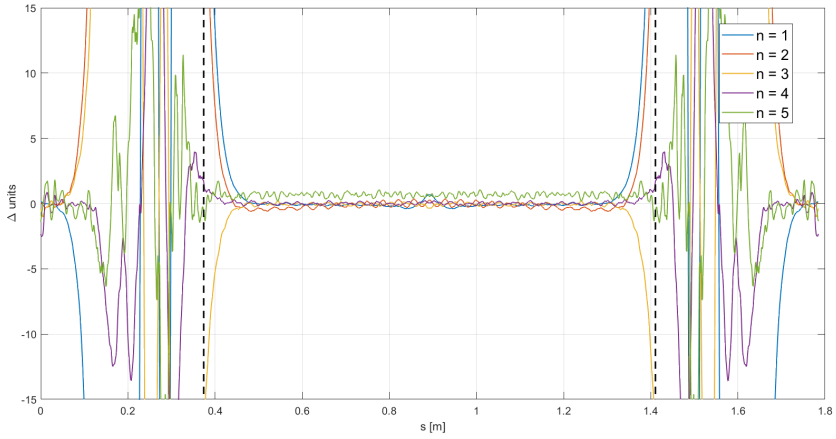

Figure 4.12: Illustration of the difference expressed in field units between the multipole coefficients determined with the Fourier series expansion and the field harmonics evaluated with a suitable Taylor series expansion. The black dashed lines indicate the points at $\pm 18°$, near the beginning of the dipole heads. In general, the parameter n refers to the field harmonic distributions and, in this graph, $n = 1$ coincides with the difference evaluated for the dipole component and so on.

the multipole coefficients evaluated with the Fourier series expansion of the radial field component and the field harmonics calculated with a suitable Taylor series expansion of the flux density at the horizontal median plane confirms that the description of the magnetic field in a strongly bent magnet based on cylindrical multipoles, already assessed globally incorrect, leads to an unclear interpretation of the results.

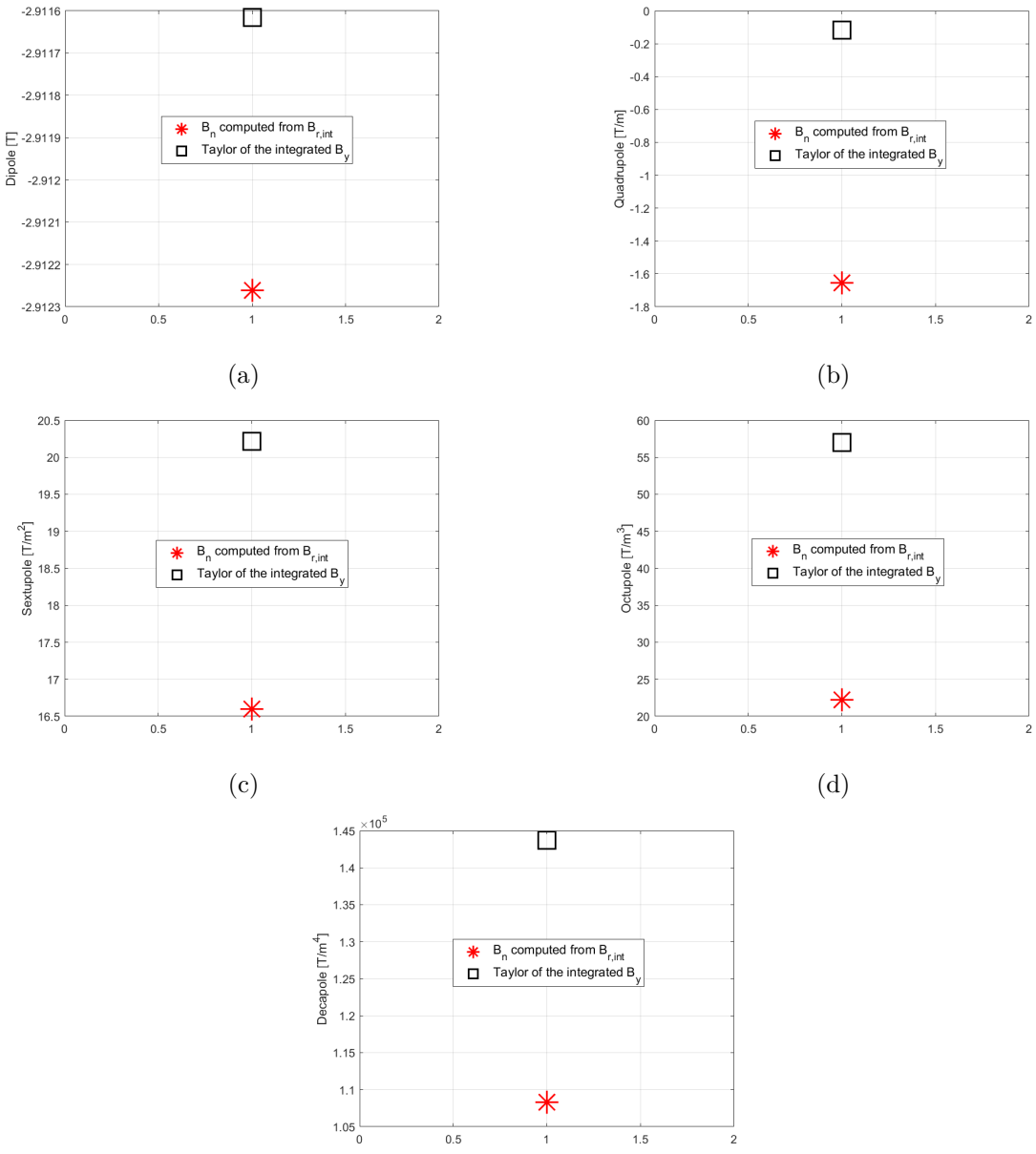

(a) (b) (c) (d) (e)

Figure 4.13: (a) Comparison between the dipole component evaluated with Fourier expansion of $B_{r,int}$ and with Taylor expansion of the integrated field. (b) Comparison between the quadrupole component evaluated with Fourier expansion of $B_{r,int}$ and with Taylor expansion of the integrated field. (c) Comparison between the sextupole component evaluated with Fourier expansion of $B_{r,int}$ and with Taylor expansion of the integrated field. (d) Comparison between the octupole component evaluated with Fourier expansion of $B_{r,int}$ and with Taylor expansion of the integrated field. (e) Comparison between the decapole component evaluated with Fourier expansion of $B_{r,int}$ and with Taylor expansion of the integrated field.

Chapter 5

Tracking and Taylor Agreement

The work presented in this chapter is also reported in [27].
The description of the short and strongly bent dipole magnets in traditional beam optics codes requires appropriate examination. Generally, the magnets in transfer lines are described with a linear hard edge model, where the magnetic field is constant inside the magnets and null outside. This approximation is an appropriate representation for long accelerator magnets as long as the length of the magnet's heads is negligible with respect to the magnetic length and the non-linear components are neglected. Nevertheless, these constraints are not valid for short magnets with a relatively large aperture such as the ones involved in the gantry design. Indeed, the coil's heads represent the 25% of the total length of the magnet and the transition of the field cannot be approximated as a hard edge model. Moreover, the strong curvature of the dipole introduces non-linear components that have to be considered in the analysis.

An algorithm based on particle tracking inside the 3D magnetic field map of the combined function dipole is employed to extract the set of linear and non-linear magnets parameters [30]. First, with a least-square fitting algorithm, a linear transfer matrix can be extracted using the initial and the final coordinates of the tracked particles. Second, an optimization algorithm is used to match the calculated matrix with the main parameters of a sequence of known linear optics elements (such as combined function dipole, drifts and dipole edges). Then, these results are used as starting point to evaluate the magnet's non-linear components including thin lenses in the above-mentioned sequence. The high-order field components of the thin lenses are used as a base to minimize the differences in particles' position and divergence between the tracking in the 3D magnetic field map and the developed non-linear model. Finally, the described procedure is benchmarked with the calculation of the multipole coefficients of the magnetic field through a suitable Taylor series expansion in the case of magnets with a mid-plane symmetry [19], [21]. The produced transport matrices can be used in accelerator codes, such as MAD-X, to feasibly describe the beam transport. The MAD-X (Methodical Accelerator Design) project is a simulation tool for charged particle optics design in accelerators and beamlines [34]. In this context, the program is used to simulate the transport of the beam through the transport line.

The 3D magnetic field map, calculated with the Opera Simulation Software [26] and

illustrated in Fig. 3.1a, is the input for the investigation process. The analysis of the field map will be thoroughly described hereafter.

5.1 Field Components Evaluation with Particle Tracking

The particle beam is propagated in the magnet by using the Runge-Kutta-Fehlberg method, an algorithm useful for the numerical solution of ordinary differential equations (ODE). As introduced in Sec. 3.5, the Lorentz force is integrated and divided by the relativistic mass $m\gamma$ of the particle and then, the velocities of the particles at different instants are determined as reported in Eq. 3.11:

$$\int_{T_{i-1}}^{T_i} \frac{d\mathbf{v}(t)}{dt}\, dt = \int_{T_{i-1}}^{T_i} \frac{q}{m\gamma}(\mathbf{v}(t) \times \mathbf{B}\, dt, i = 1, ..., n$$

where q is the particle charge, m and v are respectively the mass and the velocity of the particle, γ is the relativistic Lorentz factor. The relative and the absolute error tolerances of the Runge-Kutta algorithm are imposed both equal to 10^{-9}. The space coordinates are consequently evaluated from the velocities.

To correctly reproduce the transport properties of the magnet, a local reference system co-moving with the reference particle has to be determined. An illustration of the co-moving system is reported in Fig. 5.1.

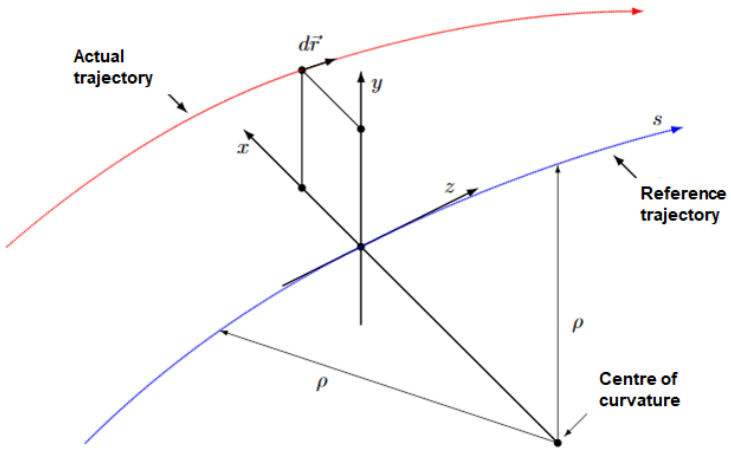

Figure 5.1: Representation of the co-moving system. The s-axis is tangent to the reference trajectory [34].

The reference particle is the one that performs the nominal bending angle of 45° and its orbit is selected as the reference trajectory. To calculate the local system co-moving with the reference particle, the traslation and rotation transformations are applied to the particle's global coordinates for each point of the tracking. The traslation brings the reference system on the reference particle and the rotation is applied to have the longitudinal axis of the motion coincident with one of the reference particle velocity.

The particles' coordinates in the co-moving system are interpolated in the longitudinal direction to obtain the distribution of the particles in the motion transverse plane of the reference particle [30]. The phase-space divergence is evaluated by considering the coordinates difference of two successive points and then, dividing by the space travelled along these ones.

Firstly, it is assumed that the transport through the magnetic field map can be represented using a lattice composed of linear magnetic elements. Considering that the transverse dimension of the beam is small compared to the radius of curvature of the particle trajectory, the y-component of the magnetic flux density $B_y(x)$ can be expanded in the proximity of the reference trajectory on the median plane as reported in Eq. 2.18. The latter equation terms can be multiplied by q/p, where q is the particle charge and p is the particle momentum, to obtain [20]:

$$\frac{q}{p}B_y(x) = \frac{1}{\rho} + kx + \frac{1}{2!}mx^2 + \frac{1}{3!}ox^3 + ... \tag{5.1}$$

where the term $k(x) = \frac{q}{p}\frac{dB_y}{dx}x$ is the normalized quadrupole gradient and $\rho = \frac{p}{qB_0}$ is the trajectory curvature radius. The terms m and o are respectively the normalized sextupole and octupole gradients. Generally, the design of a beamline is performed with linear beam optics and hard edge model representation. The beam optics is defined as linear where the forces are constant (dipole term) or increase linearly with the transverse displacement (quadrupole term).

The motion equations are reported, after some manipulation, as [20]:

$$\begin{cases} x''(s) + [\frac{1}{\rho^2} - k(s)]x(s) = \frac{1}{\rho}\frac{\Delta p}{p} \\ \\ y''(s) + k(s)y(s) = 0 \end{cases} \tag{5.2}$$

where $x''(s) = \frac{d^2x}{ds^2}$ and $y''(s) = \frac{d^2y}{ds^2}$ are respectively the second derivative of x and y with respect to s, and the term $\frac{\Delta p}{p}$ is the relative momentum deviation assumed to be null. The motion equations' solutions describe the particles' oscillation around the reference trajectory.

The propagation of the particles through magnetic elements can be described with a series of transfer matrices of each element:

$$X_{final} = M_T X_0 \tag{5.3}$$

where the transfer matrix $M_T = \prod_i M_i$ and i indicates the number of magnetic elements in the transfer line, X represents the vector that contains the particle coordinates in phase space x, p_x, y, p_y for each point. The coordinates of the particles in the co-moving system are used to obtain the coefficients of the transfer matrix M_T. Knowing X_{final} and X_0, M_T can be estimated with the least square method. Specifically, the optimization algorithm is used to evaluate the best configuration of the transfer matrix coefficients that minimize $||X_{tracking} - M_{model}X_0||$. The calculated transfer matrix is used to determine the magnet parameters in terms of the usual transfer matrices employed in the accelerator

optics codes. The linear model of the magnetic field map is performed as a symmetric set of elements including combined function dipole, dipole edges including the fringe field and drifts on each side of the dipole. These linear element matrices are evaluated by solving the motion equations Eq. 5.2.

The total transfer matrix of the 3D magnetic field map can be represented as:

$$M_{model} = M_{drift,2} \cdot M_{edge} \cdot \tilde{M} \cdot M_{edge} \cdot M_{drift,1} \tag{5.4}$$

where $\tilde{M}$ is the transfer matrix of the combined function dipole. To obtain the coefficients of the transfer matrix M_{model} which are the best-reproducing set of the matrix M_T calculated with the particle tracking, an optimizer is used. The principle of the non-linear optimization code is based on varying some free parameters to minimize the sum of squared differences of each matrix coefficient.

A more accurate representation of the magnetic field map is performed by considering the non-linear field components. In this case, the matrix notation cannot be used, thus the non-linear components are retrieved by employing another optimization function. Two multipolar lenses are added to the linear optic system previously described and located at the dipole edges. Moreover, a sextupole component is added inside the combined function dipole. A schematic configuration of the magnetic system is illustrated in Fig. 5.2.

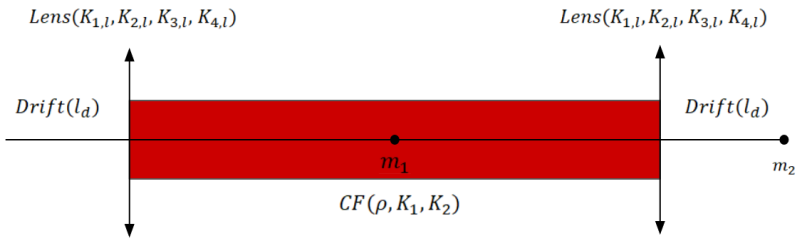

Figure 5.2: Illustration of the magnetic system implemented in MAD-X. The longitudinal axis is represented with the black line, the multipolar lenses are reported with the black rows and the combined function dipole is shown with the red rectangle.

To perform particle tracking through the beamline, the PTC module is used in MAD-X. The Polymorphic Tracking Code (PTC) is a library for integrating the equations of orbital spin motion for particles in modern accelerator and storage rings [35].

The results of the particle distributions obtained with the PTC code and the particle tracking based on the Runge-Kutta algorithm are finally matched by changing the multipolar lens components and the sextupole component in the dipole at each step to find the optimal configuration.

5.2 Analysis Results

As a reminder, the analysed 3D magnetic field map represents a 4 T combined function dipole with a bending radius of 1.65 m and a bending angle of 45°. The total length of

the map and the magnetic length of the dipole are respectively equal to 1.78 m and 1.3 m. A detailed description of the field map characteristic is also reported in Sec. 2.3. To evaluate the beam transport along the optic line that simulates the magnetic field map, PTC is employed and, specifically, the linear and the non-linear optic system approximations are evaluated. The PTC tracking results are then compared with the ones directly retrieved from the magnetic field map performing the tracking based on the Runge-Kutta algorithm.

The beam used for the analysis is a Gaussian beam with $\beta_x = \beta_y = 10$ m, $\alpha_x = \alpha_y = 0$ rad and $\epsilon_{rms,x} = \epsilon_{rms,y} = 5\pi$ mm mrad, that represents a possible realistic beam distribution at the entrance of such a dipole. The energy of the particle that performs the bending angle of 45° is equal to 428.5 MeV/u and all the particles of the initialized beam are set to the same energy. The final particle distribution is compared to the one evaluated with the Runge-Kutta tracking along the magnetic field map.

In the case of a non-linear approximation, the multipolar thin lenses and the sextupole component inside the dipole are considered as shown in Fig. 5.2. The multipolar lenses combined with the sextupole component along the thick dipole reproduce satisfactorily the behaviour of the particle in the magnetic field map and the beam distributions are represented in Fig. 5.3. The maximum differences between the coordinates obtained with Runge-Kutta tracking performed on the field map and the PTC tracking performed in MAD-X are reported in Tab. 5.1.

Maximum absolute difference	**Non-Linear system - Gaussian beam**
$\Delta x[mm]$	$7.41{\cdot}10^{-2}$
$\Delta x'[mrad]$	$4.88{\cdot}10^{-2}$
$\Delta y[mm]$	$6.49{\cdot}10^{-2}$
$\Delta y'[mrad]$	$5.23{\cdot}10^{-2}$

Table 5.1: Maximum difference for the phase-space coordinates.

As a final analysis, the field components determined with the tracking based on the Runge-Kutta algorithm are benchmarked against the multipoles obtained through the Taylor expansion analysis of the magnetic field map along the reference particle trajectory thoroughly described in Sec. 3.2 and Sec. 3.3. First, the average integral values of the dipole and the quadrupole components are evaluated considering only the region of the thick dipole approximately identified at ±22.5°, whereas the sextupole component along the dipole is not taken into account; second, the integrals up to the decapole component are calculated considering the magnetic field map from the beginning (out of the magnet) to the middle to obtain the field components of the multipolar thin lenses. In this case, the calculation of the integral as reported in Eq. 3.2 is imposed by the fact that the multipolar lenses have zero length. The non-linear optic system illustrated in Fig. 5.2 is then adapted to the Taylor expansion analysis and, since the dipole fringe fields may require further investigation in the Taylor analysis, they have been removed from the system. Furthermore, the sextupole component along the thick dipole is not considered since this component is evaluated only in the multipolar lenses. The Taylor

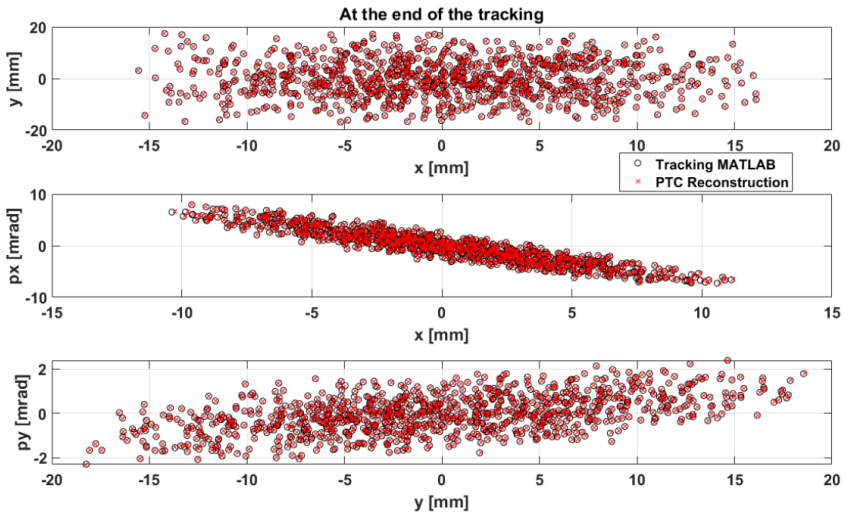

Figure 5.3: Representation of space and divergence distributions at the end of the non-linear magnetic system. The particle coordinates evaluated by using the PTC track are represented in red, while in black are illustrated the coordinates retrieved with Runge-Kutta tracking.

series expansion is evaluated along the reference trajectory approximated with an arc of a circle with a bending radius ρ=1.65 m and two straight sections each one long l_d= 0.24 m. The length of the segment ΔL selected for the Taylor expansion analysis is equal to 21.6 mm in order to be coherent with the beam size analysed with the particle tracking and to remain inside a region in which, as a first approximation, the magnetic field behaves properly. The results obtained with the two analysis are reported in Tab. 5.2.

Magnet coefficient	**Taylor Analysis**	**Runge-Kutta Tracking**
K_1 [T/m]	0.125	0.123
K_2L [T/m^2 m]	-17.4	-17.7
K_3L [T/m^3 m]	-66	-57
K_4L [T/m^4 m]	-7.5·10^3	-93 ·10^3

Table 5.2: Values of the magnetic coefficients calculated with the Taylor expansion analysis and tracking based on Runge-Kutta algorithm. The coefficient K_1 is the quadrupole component inside the thick dipole. The parameters with L represent the integrated multipolar components from sextupole component K_2L to decapole component K_4L.

The maximum differences between the coordinates calculated with the two sets of field components shown in Tab. 5.2 are reported in Tab. 5.3.

To properly evaluate the difference of the field components values retrieved respectively with the tracking based on the Runge-Kutta algorithm and with the Taylor series expansion approach, the results are converted into field units by employing the conversion formula reported in Eq. 2.19 considering the radius of 21.6 mm. In the conversion

Max difference	Taylor Analysis	Adapted Non-Linear system
$\Delta x[mm]$	$3.01{\cdot}10^{-1}$	$2.93{\cdot}10^{-1}$
$\Delta x'[mrad]$	$1.21{\cdot}10^{-1}$	$1.09{\cdot}10^{-1}$
$\Delta y[mm]$	$3.27{\cdot}10^{-1}$	$2.69{\cdot}10^{-1}$
$\Delta y'[mrad]$	$1.06{\cdot}10^{-1}$	$1.01{\cdot}10^{-1}$

Table 5.3: Maximum difference for the phase-space coordinates.

formula, B_N is the dipole field component and it is used to normalize the retrieved coefficients respectively evaluated with the tracking based on the Runge-Kutta algorithm and with the Taylor expansion analysis. The difference of the field components reported in Tab. 5.2 is listed in terms of field units in Tab. 5.4.

Absolute Unit Difference	Value
$\Delta k_{1,d}[unit]$	0.35
$\Delta k_{2,l}[unit]$	0.19
$\Delta k_{3,l}[unit]$	0.03
$\Delta k_{4,l}[unit]$	1.93

Table 5.4: Difference in terms of units among the field components evaluated using the Taylor expansion analysis and the Runge-Kutta tracking. The dipole components difference is not considered in the table. The subscript d represents the coefficients in the thick dipole and the subscript l indicates the components considered in the multipolar lenses.

The differences evaluated between the field components are below two field units. Therefore, as a first approximation, the Taylor expansion method can be employed to analyse the 3D magnetic field maps. The evaluated field components are comparable with the magnet coefficients calculated by the particle tracking based on the Runge-Kutta algorithm. In conclusion, the Taylor series expansion analysis allows an effective non-linear description of the magnetic field map.

Chapter 6

Field Quality in Straight Magnet

The magnetic field quality analysis is performed on a straight magnet in order to verify the consistency between the Taylor series expansion and the Fourier series expansion. The straight dipole is designed in Opera Simulation Software. The model of the dipole's coils is the straight version of the one described in Sec. 2.3. The design of the iron yoke is then built after importing the coils inside the Opera Simulation Software and the yoke material is the same employed in the modelling of the curved dipole. Thanks to the symmetry of the magnet, the analysis can be performed just considering one-fourth of the iron yoke. The magnetic field is imposed normal with respect to the ZX plane and tangent to the XY plane.

The 3D magnetic field map for the straight dipole is evaluated and the data for the magnetic field components B_x, B_y, B_z are determined. The model of the straight magnet designed in Opera Simulation Software is shown in Fig. 6.1, where the 3D coils are illustrated in red and the iron yoke is represented in green.

The behaviour of the magnetic field in the middle section of the magnet is illustrated in Fig. 6.2 and it is expressed in tesla. The value of the magnetic field in the dipole aperture is equal to 4 T and it decreases going outwards down to 0 T at a sufficient distance from the dipole.

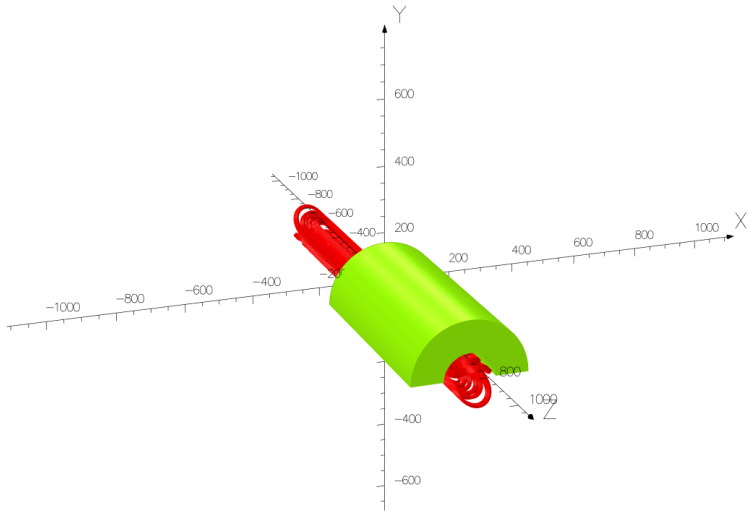

Figure 6.1: Illustration of the straight magnet modelled in Opera Simulation Software.

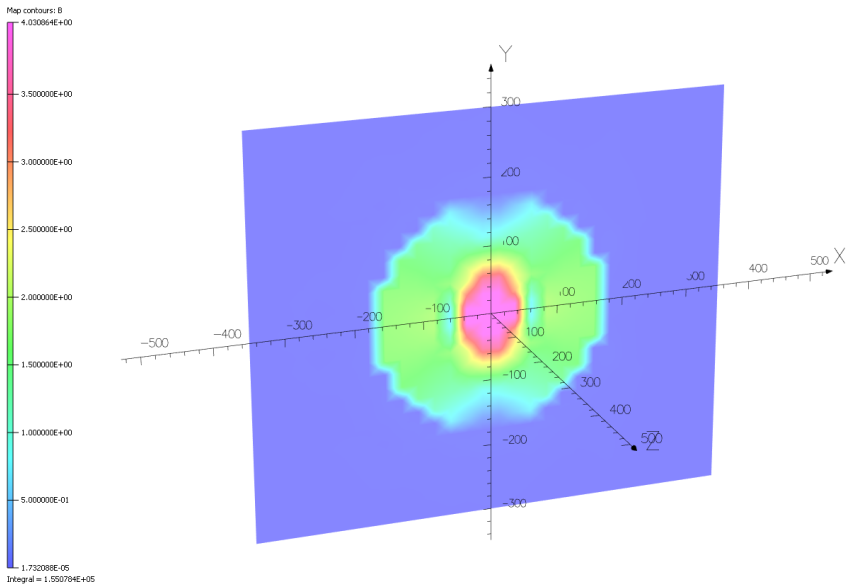

Figure 6.2: Representation of the magnetic field behaviour calculated in Opera Simulation Software.

6.1 Taylor Expansion Analysis

The particle trajectory in the case of a straight magnet is approximated with a straight line. It is fundamental to point out that the straight line does not represent the real orbit of an ideal carbon ion particle with a maximum kinetic energy of 430 MeV per nucleon, however, it is an appropriate choice for the analysis purpose. The total length of the field map is roughly 1.78 m and this is chosen so that the field components at the end of the magnetic field map are roughly null. The length of the straight line is set in order to remain inside the magnetic field map. The 3D magnetic field map evaluated in Opera Simulation Software and the straight line constructed to perform the field quality analysis are illustrated in Fig. 6.3.

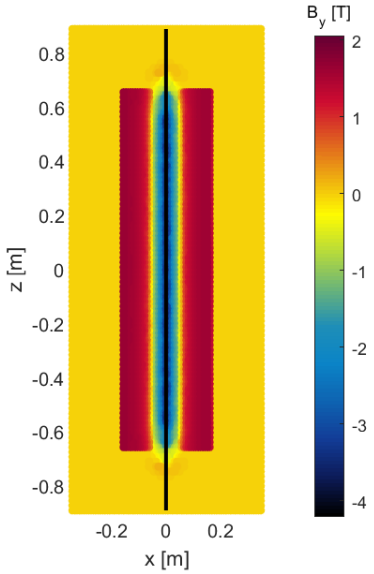

Figure 6.3: Illustration of the magnetic field map calculated in Opera Simulation Software where the colour bar on the right represents the values of the y-component of the magnetic field B_y in tesla; the black straight line is the path selected for analysing the magnetic field quality.

The field components are illustrated in Fig. 6.4 and the bending of the particles on the XZ plane occurs thanks to the action of the y-component of the magnetic field. The component B_y decreases after intercepting the heads of the dipole. The current and the coils' model are the same employed in the case of the bent dipole described in Sec. 2.3.

The y-component of the magnetic flux density $B_y(x)$ and its derivatives with respect to x are assessed on a set of segments perpendicular to the straight line. The set of perpendicular segments is illustrated in Fig. 6.5.

Specifically, the magnetic flux density $B_y(x)$ can be expanded in the median plane about an axis at $x_0 = 0$ as shown in Eq. 2.18. The length of each segment, equal to 21.6 mm, is imposed to remain inside a region in which, as a first approximation, the magnetic field behaves properly. In the case of accelerator magnets, the extension of this

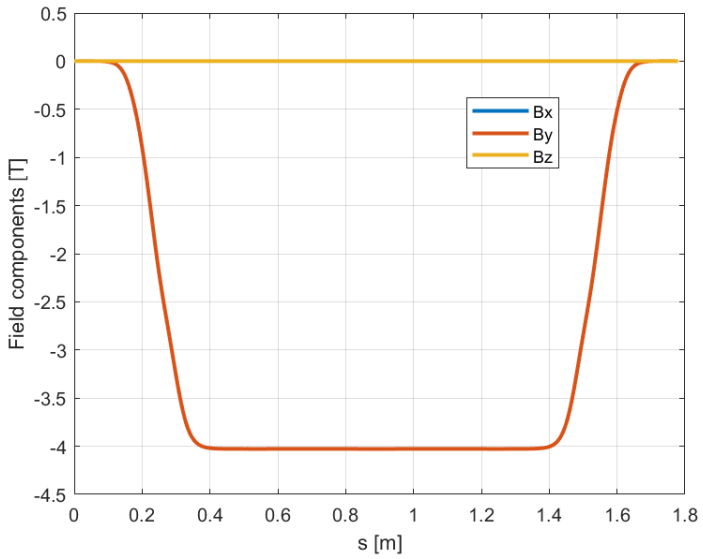

Figure 6.4: Representation of the magnetic field components in tesla plotted with respect to the longitudinal coordinate s.

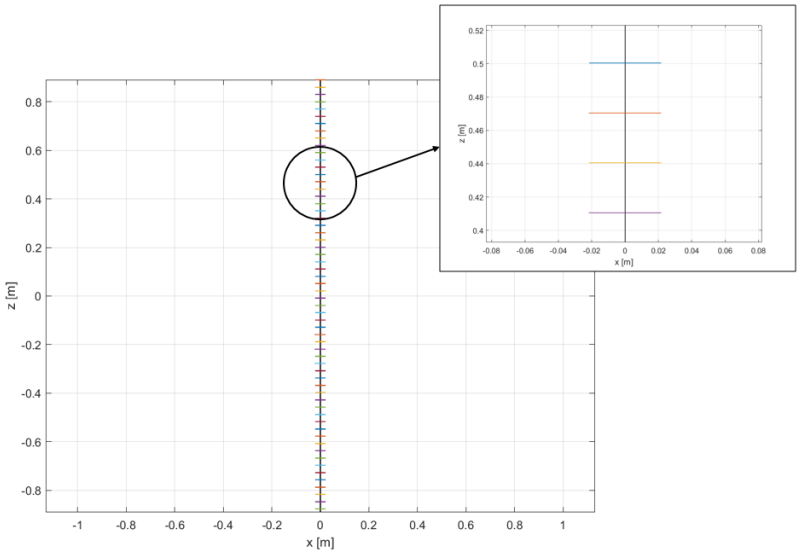

Figure 6.5: Illustration of the straight line on which a set of perpendicular segments is defined.

magnetic field region is conventionally defined as two-thirds of the aperture radius. The interpolation of the y-component of the magnetic field B_y with respect to the local x-coordinate identified on the segment itself is calculated using a polynomial curve fitting as thoroughly described in Sec. 3.2. The query points x are identified on the perpendicular

segments and the y data are the values of the magnetic field evaluated with the Opera Simulation Software. To define the multipole coefficients of the field B_y on each segment, the coefficients determined by interpolating are multiplied for the factorial of $(n-1)$ where n is the degree of the polynomial term. To remain consistent with the field quality analysis performed with the bent dipole, the polynomial degree n is set equal to six.

The field components are represented in Fig. 6.6 and plotted with respect to the reference path s approximated with a straight line.

The main field component, shown in Fig. 6.6, takes on the value of 4 T in the body of the straight dipole and decreases after having reached the coils' head down to 0 T, i.e. a field-free region. The quadrupole component presents evident peaks remaining anyway above -0.03 T/m. Indeed, the quadrupole coefficient converted in field units is below one unit and this result confirms the optimization of the magnet as a pure dipole in 2D cross-section. The octupole component indicates strong oscillations, while the even-derivatives, such as the sextupole and the decapole components, present a less visible oscillation.

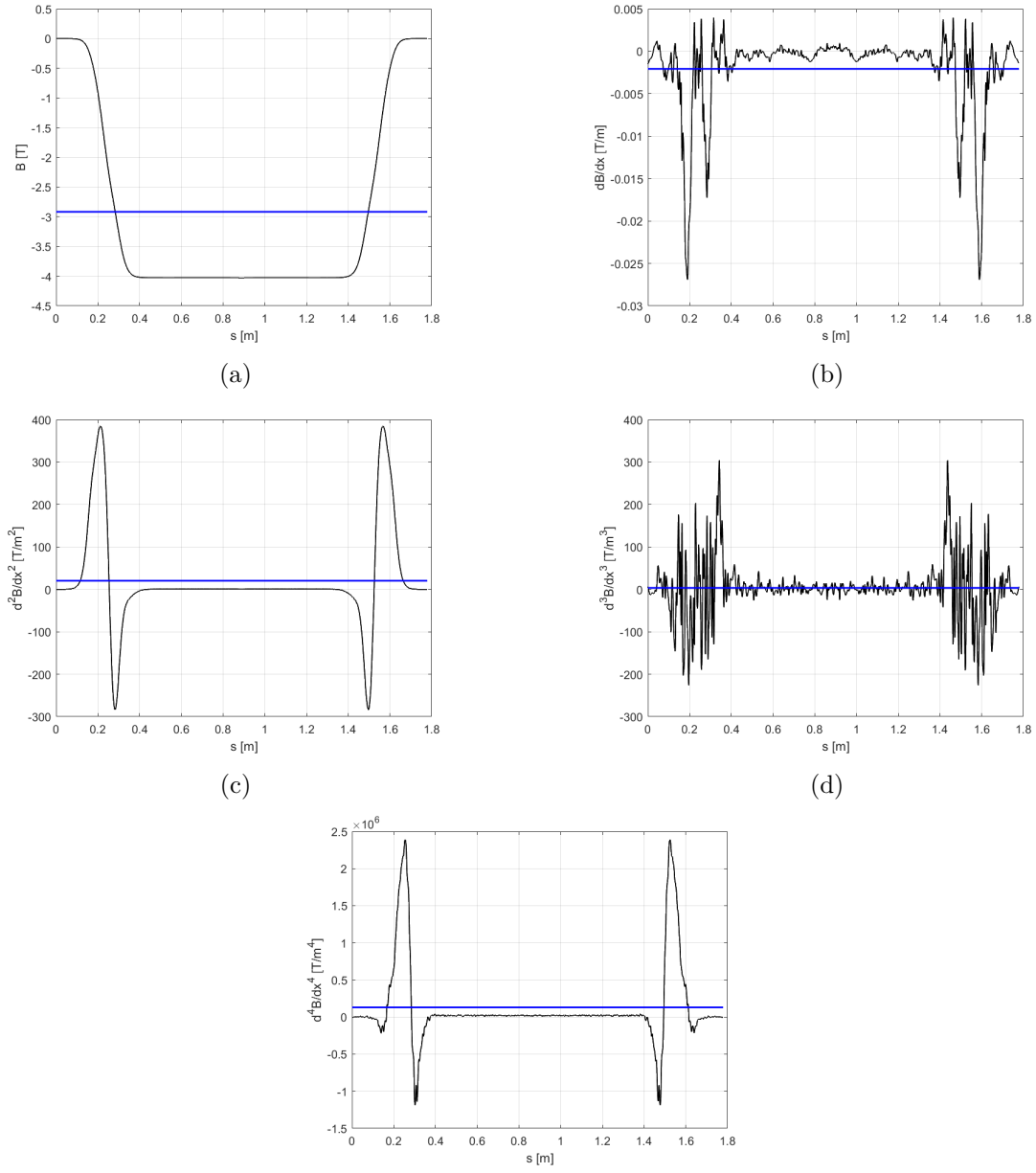

Figure 6.6: (a) The dipole component plotted along the longitudinal coordinate. (b) The quadrupole component plotted along the longitudinal coordinate. (c) The sextupole component plotted along the longitudinal coordinate. (d) The octupole component plotted along the longitudinal coordinate. (e) The decapole component plotted along the longitudinal coordinate. In all figures, the blue line represents the values of the average integral calculated by normalizing the integral results for the chosen path.

To evaluate the n-poles components for the complete straight magnet, the integral of the multipole components is calculated using Eq. 3.2, where s, in this case, represents the longitudinal coordinate. The integration results are illustrated in Tab. 6.1.

Integral of Taylor coefficients				
Dipole $[Tm]$	**Quadrupole** $[T/m\ m]$	**Sextupole** $[T/m^2\ m]$	**Octupole** $[T/m^3\ m]$	**Decapole** $[T/m^4\ m]$
-5.19	-0.004	36.19	6.19	2.32×10^5

Table 6.1: Results obtained by the integral of the multipole coefficients evaluated with Eq. 3.2 considering the longitudinal coordinate s.

The average integral is calculated by normalizing the results of the integrated multipole coefficients for the length of the straight line used for the analysis and the evaluated values are shown in Tab. 6.2.

Average integral of Taylor coefficients				
Dipole $[T]$	**Quadrupole** $[T/m]$	**Sextupole** $[T/m^2]$	**Octupole** $[T/m^3]$	**Decapole** $[T/m^4]$
-2.91	-0.002	20.33	3.47	1.30×10^5

Table 6.2: Average integral of the multipole coefficients calculated by normalizing for the length of the straight line.

The quadrupole gradient of the straight magnet model is significantly lower than the one evaluated in the case of the strongly curved dipole where the bending of the magnet coils introduces a gradient of 0.12 T/m in the horizontal plane. The quadrupole component of the straight magnet is effectively equal to 0.002 T/m and this value confirms the optimization of the magnet as a pure dipole in the 2D coil cross-section.

However, the coils' head introduces high-order components that result in a non-negligible value of the average integral especially for the sextupole and the decapole components. In any case, the average integrals evaluated by normalizing the integral of the multipole coefficients for the length of the straight line are consistent with the values illustrated in Fig. 6.6 with the blue lines.

The conversion formula (see Eq. 2.19) is used to convert the results of the integrated multipole coefficients in field units. The outcomes are reported in Tab. 6.3 and the value of B_N, i.e. the main field component, is the integrated dipole field equal to -5.19 T.

The sextupole component requires further optimization to respect the limit of 10 units imposed for the analysis. However, the other high-order multipole coefficients fulfil the requirements.

Multipole coefficients in field units				
Dipole [-]	**Quadrupole** [-]	**Sextupole** [-]	**Octupole** [-]	**Decapole** [-]
10000	0.15	-16.26	-0.02	-4.04

Table 6.3: The values of the multipole coefficients converted in field units using the conversion formula Eq. 2.19. The main field component B_N used in the formula is the value of the integrated dipole component.

6.2 Fourier Expansion Analysis

The field quality analysis of the straight magnet is also performed by considering the Fourier series expansion of the radial component of the magnetic flux density. The Fourier expansion approach is detailed described in Sec. 2.1. As a reminder, the 3D magnetic field map evaluated with the Opera Simulation Software is displayed in Fig. 6.3. The trajectory selected for the field quality analysis is a straight line, a reasonable approximation for the assessment purpose. For accelerator magnets, the domain of the problem is generally chosen as a circle with a radius of two-thirds of the aperture radius [19]. The reference radius r_0 is set equal to 21.6 mm in order to remain inside a region where the field behaves suitably and to guarantee the comparability with the multipole coefficients evaluated by the Taylor series expansion of the magnetic flux density at the median plane. The field harmonics A_n and B_n require the calculation of the radial field component of the magnetic flux density. First, the definition of a set of circles perpendicular to the straight line is performed. The radial field component B_r of the magnetic flux density at a reference radius r_0 as a function of the angular position is evaluated on each circle and then, it is expressed with the Fourier series expansion. The radial field component is assessed on a set of circles built perpendicularly with respect to the straight line. These circles are illustrated in Fig. 6.7 where the colour bar indicates the values of the radial field component in tesla.

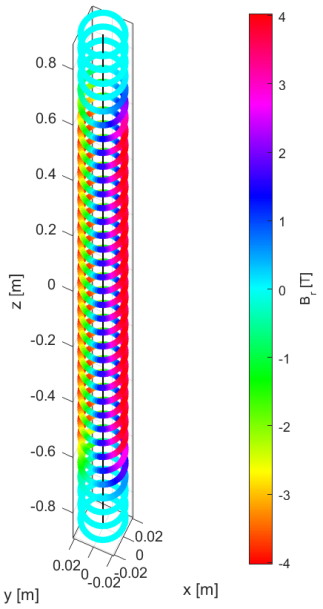

Figure 6.7: llustration of the set of circles transverse to the straight line. The colour bar on the right indicates the values of the radial field component B_r in tesla.

The behaviour of the radial field component on each circle confirms that the field components at the end of the magnetic field map are roughly null. In computational

practice, the component B_r is evaluated at N discrete points in the interval [0,2π) and the multipole coefficients $A_n(r_0)$ and $B_n(r_0)$ are determined by using Eq. 4.3 and Eq. 4.4 reported below.

$$A_n(r_0) \approx \frac{2}{N} \sum_{k=0}^{N-1} B_r(r_0, \varphi_k)\ cos\ n\varphi_k$$

$$B_n(r_0) \approx \frac{2}{N} \sum_{k=0}^{N-1} B_r(r_0, \varphi_k)\ sin\ n\varphi_k$$

The skew component $A_n(r_0)$ is supposed to be null due to the symmetry of the field about the horizontal median plane. The distributions of the normal multipole components $B_n(r_0)$ are represented in Fig. 6.8. The coefficient $n = 1$ represents the dipole field. The other field components are illustrated by normalizing the multipoles for the reference radius r_0 raised to $n - 1$.

The trend of the dipole component is unchanged from the y-component of the magnetic field illustrated in Fig. 6.4 and the value of the dipole field is confirmed at 4 T in the dipole's body. The high-order multipole coefficients present less pronounced variations with respect to the field harmonics represented in Fig. 6.6. The quadrupole and the decapole components respectively illustrated in Fig. 6.8b and Fig. 6.8e have an entirely comparable trend with the same field components shown in Fig. 6.6b and Fig. 6.6e. However, the sextupole and the octupole components shown in Fig. 6.8c and Fig. 6.8d present some trend differences with respect to the components displayed in Fig. 6.6c and Fig. 6.6d but the mean values of the respective B_n component normalized for the reference radius raised to $n - 1$ are perfectly consistent with the average integral of the multipole components evaluated with the Taylor series expansion.

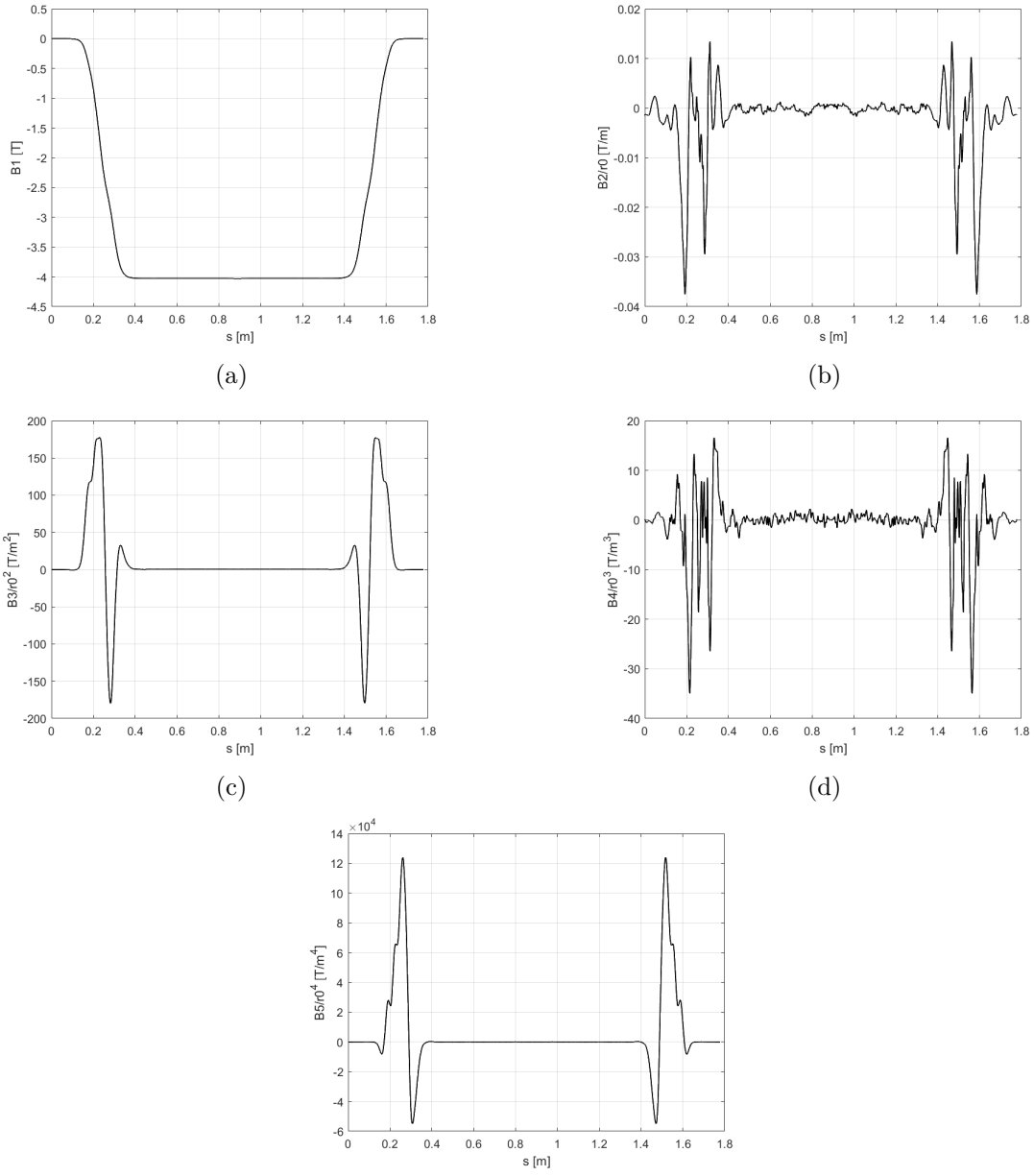

Figure 6.8: (a) Representation of the dipole component B_1 in T plotted with respect to the straight line. (b) Representation of the quadrupole component B_2 in T/m plotted with respect to the straight line. (c) Representation of the sextupole component B_3 in T/m^2 plotted with respect to the straight line. (d) Representation of the octupole component B_4 in T/m^3 plotted with respect to the straight line. (e) Representation of the decapole component B_5 in T/m^4 plotted with respect to the straight line.

The mean values of the normal multipole components determined with the Fourier series expansion are then represented in Tab. 6.4 considering that each normal multipole component is divided by the reference radius r_0 raised to $n-1$.

Mean value of the B_n coefficients				
Dipole $[T]$	**Quadrupole** $[T/m]$	**Sextupole** $[T/m^2]$	**Octupole** $[T/m^3]$	**Decapole** $[T/m^4]$
-2.91	-0.002	20.18	-3.56	1.32×10^5

Table 6.4: Results retrieved by calculating the mean value of the normal multipole coefficients B_n divided by the reference radius r_0 raised to $n-1$.

The results presented in Tab. 6.2 and Tab. 6.4 are perfectly in accordance as a confirmation that the two discussed methods for determining the field harmonics are both valid in case a straight magnet configuration is analysed.

The retrieved results are converted in field units (see Eq. 2.19) and reported in Tab. 6.5. In this case, the value of B_N is the mean value of the dipole component equal to -2.91 T.

Multipole coefficients in field units				
Dipole [-]	**Quadrupole [-]**	**Sextupole [-]**	**Octupole [-]**	**Decapole [-]**
10000	0.15	-16.14	0.02	-4.11

Table 6.5: The values of the multipole coefficients converted in field units using Eq. 2.19. The main field component B_N used in the formula is the mean value of the dipole component.

Moreover, the absolute unit difference of the multipole coefficients calculated with the Taylor series expansion and the field harmonics evaluated with the Fourier expansion of the radial field component is reported in Tab. 6.6. The difference results demonstrate that both methods are suitable for a correct analysis of the field quality in the case of a straight magnet.

Finally, the unit difference between the multipole coefficients respectively evaluated with the Fourier and Taylor expansion methods (see Eq. 4.4) is graphically illustrated in Fig. 6.9. In the body of the magnet, the results show a great agreement while the differences of the field harmonics in the coils' heads are affected by noticeable inaccuracies. The reason can be related to the fact that the expansion of the field with a Fourier series does not provide understandable results in the dipole heads where the field variation in the axial direction is relevant. However, in the case of symmetric fields or for longitudinal field component that has dropped to zero [19], the integral of the field harmonics determined with the Fourier expansion are coherent with the results obtained with the Taylor expansion as also shown in Tab. 6.6.

Difference in absolute value				
Dipole [-]	**Quadrupole [-]**	**Sextupole [-]**	**Octupole [-]**	**Decapole [-]**
0	0.0034	0.1239	0.0405	0.0706

Table 6.6: The absolute unit difference of the multipole coefficients retrieved by Taylor and Fourier expansions. In particular, the difference is performed between the values reported in Tab. 6.3 and Tab. 6.5.

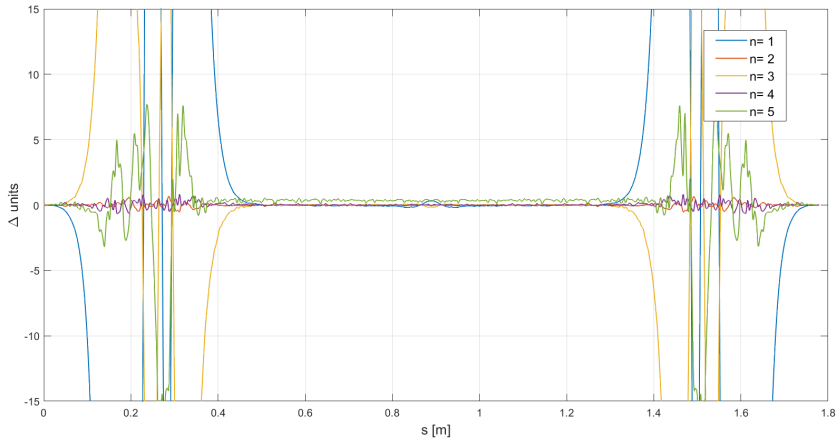

Figure 6.9: Illustration of the unit difference between the multipole coefficients determined with the Fourier series expansion and the field harmonics evaluated with a suitable Taylor series expansion. The parameter n refers to the field harmonic distributions and, in this graph, $n = 1$ coincides with the difference evaluated for the dipole component and so on.

Chapter 7

Conclusions

The purpose of this thesis is to analyze the field quality of a short and strongly bent superconducting (SC) dipole designed for a novel carbon ions gantry for hadrontherapy. The initiative has been undertaken by the National Centre for Oncological Hadrontherapy (CNAO) in the framework of the European project HITRI*plus* and a four-part collaboration with CERN (CH), INFN (IT) and MedAustron (AT).

The first step is the calculation of the magnetic field map of the curved magnet. The clinical requirement for carbon ions of a maximum kinetic energy of 430 MeV per nucleon corresponds to a beam rigidity $B\rho$ of 6.6 Tm and considering that the magnetic field B is equal to 4 T, the radius of curvature ρ results equal to 1.65 m. The 3D magnetic field map of the SC dipole involved in the field quality analysis was calculated with the Opera Simulation Software. The 2D cross-section of the magnet is optimized to be a pure dipole and then the curvature introduces a quadrupolar component. The total length of the magnetic field map is roughly 1.78 m to ensure that the field components at the end of the map are null. The sensitive issue lies in the bending transformation of the straight dipole conductors that introduces non-negligible field components with a relevant contribution of the coils' heads.

Then, a theoretical discussion on the state-of-art of field quality analysis in accelerator magnets was introduced and, specifically, two different methods were described to determine the multipole coefficients or field harmonics.

The first discussed method provides for a comparison of the field harmonics with the Taylor coefficients of a suitable series expansion of the magnetic flux density in the horizontal median plane. The analysis was performed on the orbit of the ideal carbon ion particle defined as the particle that follows the nominal geometry of the magnet and that is deflected by the nominal bending angle of 45°. The reference trajectory may be geometrically approximated with an arc of a circle with a radius of curvature ρ and two straight parts or can be computed with particle tracking based on the Runge-Kutta algorithm. In order to analyse the field quality, the multipole coefficients were assessed by interpolating the y-component of the magnetic field on a number of segments perpendicular to the reference trajectory. To retrieve the values of the n-poles components for the whole magnet, the average integral of the multipole coefficients or the field harmonics of the integrated and normalized magnetic field B_y on the horizontal segment were computed.

Both Taylor expansion approaches are consistent with each other. The results revealed that the bending of the dipole coils introduces in the horizontal plane a quadrupole gradient around 0.1 T/m in addition to the weak focusing effect which is compatible with the beam optics of the gantry. However, the sextupole component roughly equal to 16 units requires further optimization to remain within the acceptable limit of around 10 units.

Moreover, the multipoles obtained through the Taylor analysis of the magnetic field map along the reference particle trajectory were benchmarked against the field components determined with particle tracking based on the Runge-Kutta algorithm showing an agreement within a few units level. The representation of the beam distribution at the end of the field map with the Taylor expansion analysis is possible considering a relative error of the order of a few percent. Therefore, the Taylor series expansion allows the suitable representation of short and strongly bent dipoles in beam optics.

The second analysis method foresees a comparison of the integration constants in the general solution of the Laplace equation with the Fourier series expansion of the radial field component along a circle. The radial component of the magnetic flux density was assessed at a reference radius $r_0 =$ as a function of the angular position φ on a set of circles transverse to the geometrically approximated trajectory. Thus, the normal and skew multipole coefficients $B_n(r_0)$ and $A_n(r_0)$ can be determined with the integral of $B_r(r_0, \varphi)$ or with the Fourier expansion of the integrated and normalized radial field component $B_{r,int}(r_0, \varphi)$. However, concerning such dipole extremities, there is a non-negligible magnetic field in the axial direction and the multipole coefficients do not satisfy the 2D Laplace's equation. Indeed, the high-order multipole coefficients show significant differences with respect to the field harmonics determined with the Taylor expansion method. In particular, it has been observed that the difference between the multipole coefficients respectively determined with the Fourier and Taylor expansion methods was below one unit in the body of the magnet while, in the coils' heads, the same difference increased by one or two orders of magnitude.

Furthermore, the scaling law of multipole coefficients to any radius r in the body of the magnet aperture was verified in the case of strongly bent magnets. These scaling laws were used to have feedback on the extension of a region where the field behaves properly. For accelerator magnets, the extension of this field region is conventionally defined by the magnet design community as two-thirds of the aperture radius and in this case, is equal to 26.7 mm. In the body of the magnet, the agreement between the evaluation of the field harmonics with the scaling law and with the integral of the radial component is confirmed at a radius of 29.6 mm where the average unit difference of the high-order coefficients is lower than one unit.

On the one hand, the description of the magnetic field based on the multipoles evaluated with the Fourier expansion lead to a questionable interpretation of the results because the integral of the Fourier coefficients is not valid in the case of strongly curved magnets. On the other hand, the field derivatives are suitable to characterize the field and analyse the field quality requirements. The field derivatives are also directly used by beam optics calculations thus facilitating the dialogue between magnet and accelerator designers.

Finally, the field quality analysis was performed on a straight magnet designed in Opera Simulation Software to verify the consistency between Taylor and Fourier expansion methods. In such a case, the average integral of the multipole coefficients determined with the Taylor expansion and the field harmonics evaluated with the Fourier expansion of $B_r(r_0, \varphi)$ were in agreement as expected. Moreover, the results have shown that the gradient of the straight magnet was significantly lower than the one of the curved dipole where the coil bending introduces a gradient of 0.1 T/m in the horizontal plane. This outcome confirms the optimization of the magnet as a pure dipole in the 2D coil cross-section. However, the coils' head introduces high-order components.

In conclusion, the Fourier series expansion of the field components may not be appropriate for the description of the field quality in the case of short and strongly bent magnets. Nevertheless, a suitable characterization of the field, assuming a mid-plane symmetry, is possible by evaluating the field harmonics with the Taylor series expansion.

Appendix A

Convergence Analysis of the Polynomial Curve Fitting

The interpolation of the y-component of the magnetic field and the interpolation of the integrated and normalized magnetic field B_y are performed by fitting the data points with a polynomial curve. The MatLab function employed for the interpolation is *polyfit* and it is useful to find the coefficients of a polynomial that fits a set of data in a least-squares sense using the syntax $p = polyfit(x, y, n)$, where x and y are vectors containing the coordinates of the data points and n is the degree of the polynomial fit. To define the polynomial degree suitable for the field quality analysis, different degrees of the polynomial are selected to be tested in the code. Specifically, the simulations are performed considering an initial degree n equal to two up to nine. The length of the polynomial is $n + 1$ and it implies the presence of the constant term. For instance, $n = 2$ involves the possibility to get up to the sextupole component, thus truncating the expansion of the magnetic field in the vicinity of the reference trajectory as reported in Eq. A.1:

$$B_y(x) = B_0 + \left.\frac{dB_y}{dx}\right|_{x=y=0} x + \frac{1}{2!}\left.\frac{d^2B_y}{dx^2}\right|_{x=y=0} x^2 \tag{A.1}$$

The high-order multipole coefficients after the decapole component are negligible. As an example, the values of the integrated dodecapole component, converted in field units and evaluated considering the polynomial degree up to nine, are illustrated in Fig. A.1.

It is noticeable that the results retrieved for the dodecapole component are significantly lower than one unit and therefore negligible for the field quality analysis constraints.

The quadrupole and the sextupole components remain practically stable already imposing a low polynomial degree. The octupole and the decapole multipole coefficients fluctuate more than the other relevant components and these oscillation trends are reported in Fig. A.2.

Nevertheless, the polynomial degree n selected to perform the field quality analysis is set equal to six, a reasonable degree to observe a fair stabilization of the field unit results.

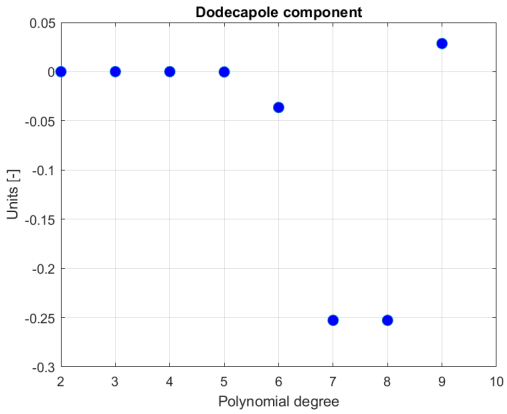

Figure A.1: Representation of the integral values of the dodecapole component considering the different degrees of the polynomial. In the x-axis are reported the field unit values and in the y-axis are shown the polynomial degrees selected for the convergence analysis.

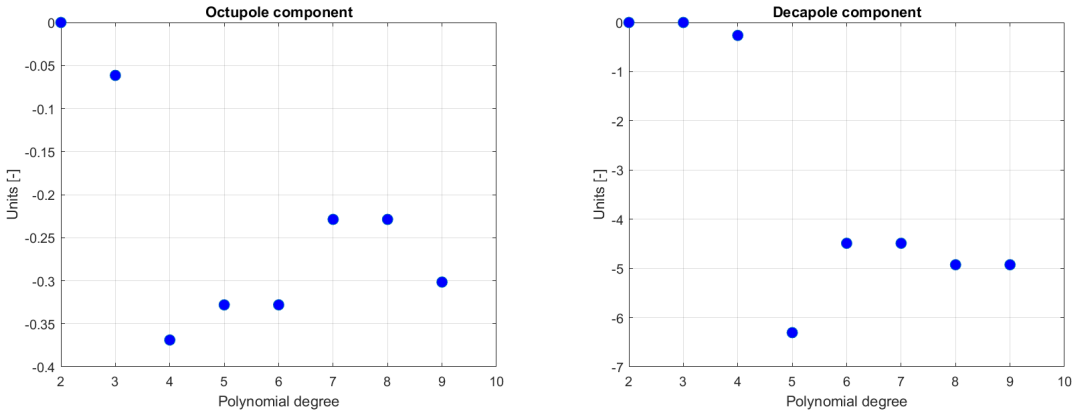

(a) (b)

Figure A.2: (a) Representation of the integral values of the octupole component, converted in field units, considering different degrees of the polynomial. (b) Representation of the integral values of the decapole component, converted in field units, considering different degrees of the polynomial. In both graphs, the x-axis reports the field unit values and the y-axis shows the polynomial degrees selected for the convergence analysis.

Bibliography

[1] Hyuna Sung et al. «Global cancer statistics 2020: GLOBOCAN estimates of incidence and mortality worldwide for 36 cancers in 185 countries». In: *CA: a cancer journal for clinicians* 71.3 (2021), pp. 209–249.

[2] Gennadii Ivanovich Klenov and Vladimir Sergeevich Khoroshkov. «Hadron therapy: history, status, prospects». In: *Physics-Uspekhi* 59.8 (2016), p. 807.

[3] Particle Therapy Co-Operative Group (PTCOG). https://www.ptcog.ch.

[4] Ugo Amaldi et al. «Accelerators for hadrontherapy: From Lawrence cyclotrons to linacs». In: *Nuclear Instruments and Methods in Physics Research Section A: Accelerators, Spectrometers, Detectors and Associated Equipment* 620.2-3 (2010), pp. 563–577.

[5] Emmanouil Fokas et al. «Ion beam radiobiology and cancer: Time to update ourselves». In: *Biochimica et Biophysica Acta (BBA) - Reviews on Cancer* 1796.2 (2009), pp. 216–229.

[6] Marco G. Pullia. «Synchrotrons for hadrontherapy». In: *Reviews of accelerator science and technology* 2.01 (2009), pp. 157–178.

[7] R. Orecchia et al. «Particle beam therapy (hadrontherapy): Basis for interest and clinical experience». English. In: *European Journal of Cancer* 34.4 (Mar. 1998), pp. 459–468.

[8] Sandro Rossi. «The National Centre for Oncological Hadrontherapy (CNAO): Status and perspectives». In: *Physica Medica* 31.4 (2015), pp. 333–351.

[9] Fondazione CNAO. http://fondazionecnao.it/it/.

[10] Enrico Felcini. *Analysis of a novel toroidal configuration for hadron therapy gantries*. Tech. rep. EPFL, 2021.

[11] V. Lante et al. «Deliverable Report JRA6.3 Conceptual design of a carbon ion gantry». In: ().

[12] M. Galonska et al. «Heidelberg heavy ion gantry experience». In: *Cockcroft Institute, Daresbury, UK* (2014).

[13] R. Fuchs, U. Weinrich, and E. Sust. «Assembly of the carbon beam gantry at the Heidelberg Ion Therapy (HIT) accelerator». In: *Proceedings of the EPAC-2008, Genoa, Italy* (2008), pp. 23–27.

[14] Y. Iwata et al. «Recent progress of a superconducting rotating-gantry for carbon-ion radiotherapy». In: *Nuclear Instruments and Methods in Physics Research Section B: Beam Interactions with Materials and Atoms* 406 (2017), pp. 338–342.

[15] S. Takayama et al. «Design and Magnetic Field Measurement of the Superconducting Magnets for the Next-Generation Rotating Gantry». In: *IEEE Transactions on Applied Superconductivity* 32.6 (2022), pp. 1–4.

[16] Ugo Amaldi et al. «SIGRUM - A Superconducting Ion Gantry with Riboni'S Unconventional Mechanics». In: (2021).

[17] Lucio Rossi et al. «A European collaboration to investigate superconducting magnets for next generation heavy ion therapy». In: *IEEE Transactions on Applied Superconductivity* 32.4 (2022), pp. 1–7.

[18] L. Rossi et al. «Preliminary Study of 4T Superconducting Dipole for a Light Rotating Gantry for Ion-Therapy». In: *IEEE Transactions on Applied Superconductivity* 32.6 (2022), pp. 1–6.

[19] Stephan Russenschuck. *Field computation for accelerator magnets: analytical and numerical methods for electromagnetic design and optimization*. Weinheim: Wiley, 2010.

[20] K. Wille and J. McFall. *The Physics of Particle Accelerators: An Introduction*. Oxford University Press, 2000.

[21] Dora Veres et al. «A new algorithm for optimizing the field quality of curved CCT magnets». In: *IEEE Transactions on Applied Superconductivity* 32.5 (2022), pp. 1–14.

[22] Lucas Brouwer et al. «3D Toroidal Field Multipoles for Curved Accelerator Magnets». In: 2017.

[23] Laura Gambini et al. «An Algorithm for Toroidal Field Harmonics Computation in Arbitrary Magnetic Configurations». In: *IEEE Transactions on Applied Superconductivity* 30.4 (2020).

[24] J. Rossbach and P. Schmuser. «Basic course on accelerator optics». In: (1994).

[25] M. Prioli et al. «Design of a 4 T Curved Demonstrator Magnet for a Superconducting Ion Gantry». In: *Accepted for publication to IEEE Transactions on Applied Superconductivity* (2023).

[26] OPERA | SIMULIA by Dassault Systémes. https://www.3ds.com/products-services/simulia/products/opera/.

[27] G. Frisella et al. «Minimization algorithms to represent strongly-bent dipoles for hadrontherapy gantry in terms of standard optics elements». In: *Submitted for publication to Physical Review Accelerators and Beams* (2022).

[28] Edwin F. Taylor, John Archibald Wheeler, et al. *Spacetime physics*. Macmillan, 1992.

[29] W. Y. Yang et al. *Applied Numerical Methods Using MATLAB®*.

[30] Gugliemo Frisella. *Investigation on C-ion Superconducting Gantry for Hadrontherapy*. Tech. rep. Universitá degli Studi di Pavia, Dipartimento di Fisica, 2021.

[31] E. Felcini et al. «Particle tracking and beam optics analysis on a toroidal gantry for proton therapy». In: *Physics in Medicine and Biology* 66.10 (2021), p. 104002.

[32] Leonardo Biccioli et al. «Boundary element method reconstruction of two-dimensional magnetic-field maps from measured boundary data in accelerator magnets». In: *IET Science, Measurement & Technology* 13.1 (2019), pp. 60–66.

[33] P. Fessia and I.R. Canseco. «3D FEM Modeling of the Moil Ends of the LHC Main Dipole». In: *IEEE Transactions on Applied Superconductivity* 16.2 (2006), pp. 1290–1293.

[34] MAD-X (Methodical Accelerator Design). https://mad.web.cern.ch/mad/.

[35] D. T. Abel. *PTC, Library User Guide*. 2011.